

Contents lists available at ScienceDirect

Petroleum Science

journal homepage: www.keaipublishing.com/en/journals/petroleum-science



Original Paper

Control of dual-function amphiphilic biochar-MoO_{3-x} catalysts with abundant oxygen vacancies for efficient extractant-free oxidative desulfurization



Xue Liang ^a, Tian-Jing Zhang ^a, Hong-Xia Yu ^a, Jie Hong ^{b, c}, Mohamed Abbas ^{b, d}, Claudia Li ^b, Sibudjing Kawi ^b, Wan-Liang Yang ^{a, b, e, *}, Mei-Song Xu ^{a, **}

- ^a School of Chemistry and Chemical Engineering, Guizhou University, Guiyang, 550025, Guizhou, China
- ^b Department of Chemical and Biomolecular Engineering, National University of Singapore, 119260, Singapore
- ^c GuiZhou University Medical College, Guizhou University, Guiyang, 550025, Guizhou, China
- d Refractories, Ceramics and Building Materials Department, National Research Centre, El- Behouth Str., 12622, Cairo, Egypt
- ^e Guizhou Provincial Double Carbon and Renewable Energy Technology Innovation Research Institute, Guizhou University, Guiyang, 550025, Guizhou, China

ARTICLE INFO

Article history: Received 10 October 2024 Received in revised form 19 December 2024 Accepted 25 February 2025 Available online 26 February 2025

Edited by Min Li

Keywords: Amphiphilic biochar catalyst **Dual-function** MoO_{3-x} Oxvgen vacancy Oxidative desulfurization Extractant-free

ABSTRACT

The development of an efficient dual-function catalytic-sorption system, which seamlessly integrates reaction and separation into a single step for extractant-free systems, represents a transformative advancement in oxidative desulfurization (ODS) process. In this work, we introduce a novel dualfunction amphiphilic biochar (Mo/CBC) catalyst, functionalized with MoO_{3-x} featuring abundant oxygen vacancies, for highly effective extractant-free ODS. The polarity of the biochar was precisely tailored by varying the amount of KOH, leading to the creation of amphiphilic carriers, Subsequent ball milling facilitated the successful loading of MoO_{3-x} onto the biochar surface via an impregnation-calcination route leveraging carbon reduction, resulting in the synthesis of amphiphilic Mo/CBC catalysts. The amphiphilic nature of these catalysts ensures their stable dispersion within the oil phase, while also facilitating their interaction with the oxidant H₂O₂ and the adsorption of sulfur-containing oxidation products. Characterization techniques, including EPR, XPS, and in situ XRD, verified the existence of abundant oxygen vacancies obtained by carbon reduction on the amphiphilic Mo/CBC catalysts, which significantly boosted their activity in an extractant-free ODS system. Remarkably, the amphiphilic Mo/ CBC catalyst displayed exceptional catalytic performance, achieving a desulfurization efficiency of 99.6% in just 10 min without extraction solvent. DFT theoretical calculations further revealed that H₂O₂ readily dissociates into two •OH radicals on the O_{vac}-MoO₃, overcoming a low energy barrier. This process was identified as a key contributor to the catalyst's outstanding ODS performance. Furthermore, other biochar sources, such as rice straw, bamboo, rapeseed oil cake, and walnut oil cake, were investigated to produce Mo-based amphiphilic biochar catalysts, which all showed excellent desulfurization performance. This work establishes a versatile and highly efficient dual-function catalytic-sorption system by designing amphiphilic biochar catalysts enriched with oxygen vacancies, paving the way for the development of universally applicable ODS catalysts for industrial applications.

© 2025 The Authors. Publishing services by Elsevier B.V. on behalf of KeAi Communications Co. Ltd. This is an open access article under the CC BY-NC-ND license (http://creativecommons.org/licenses/by-nc-nd/

1. Introduction

The widespread combustion of sulfur-containing fossil fuels poses a significant threat to both environmental and public health due to the emission of sulfur oxides (Marafi et al., 2019; Rajendran et al., 2020). In response, stringent environmental regulations have been implemented globally, intensifying the focus on fuel desulfurization. In China, for instance, the sulfur content in fuels is

^{*} Corresponding author.

^{**} Corresponding author. E-mail addresses: yangwanlianghhhh@163.com (W.-L. Yang), msxu1974@126. com (M.-S. Xu).

capped at 10 ppm, with even stricter limits anticipated (F. Liu et al., 2021; Xiong et al., 2022). Presently, hydrodesulfurization is the dominant industrial method for sulfur removal. However, its high energy demand, reliance on hydrogen, and consumption of nonrenewable resources present substantial challenges, especially in the context of global carbon neutrality objectives (Liu et al., 2023b; Wang et al., 2024; Zhou et al., 2024a, 2024b). To circumvent these challenges, alternative desulfurization technologies, such as biological desulfurization, oxidative desulfurization (ODS), extraction, and adsorption, have been developed to produce cleaner fuels (Ganiyu and Lateef, 2021; Hao et al., 2019; Torres-García et al., 2011; Wang et al., 2022; Zhang et al., 2024). Among these, ODS stands out for its mild reaction conditions and high efficiency in removing aromatic sulfides. However, the success of ODS critically depends on the development of highly efficient catalysts that can meet both performance and sustainability demands (Ye et al., 2021).

Previous investigations have explored a broad range of catalysts for ODS, including metal oxides, ionic liquids (ILs), metal organic frameworks (MOFs), polyoxometalates (POMs), heteropoly acid, noble metals, and deep eutectic solvents (Chang et al., 2020; Chen et al., 2020; A. Li et al., 2022; Liu et al., 2020; Sun et al., 2019; Yao et al., 2022; Zhang et al., 2022). Among these, molybdenum oxide (MoO_x) has attracted particular attention due to its simple synthesis, strong oxidation capacity, and unique electronic structure (Castro et al., 2017; Xiao et al., 2016; Xie et al., 2023; Yang et al., 2009). Despite these advantages, the poor dispersion of MoO_x limits its efficiency in biphasic water-oil systems, leading to the aggregation of active sites and insufficient interaction with the reaction medium (liang et al., 2019). Consequently, the development of catalysts with uniformly dispersed metal oxides is critical for achieving highly active ODS systems. Various porous supports, including transition metal oxides, SiO₂, molecular sieves, carbons, and MOFs, have been harnessed to augment the activity of MoO_x (Chen and Yuan, 2022; Guo et al., 2023b; Jiang et al., 2021; Koohsaryan et al., 2022; Safa and Ma, 2016). For instance, the immobilization of MoO_x nanoclusters on spinel-type porous nanosheets (Co₃O₄, CuCo₂O₄, ZnCo₂O₄) adeptly modulates the electronic structure of molybdenum species, leading to improved ODS performance (Liu et al., 2023). Additionally, Mo/ SiO₂-550 dendritic mesoporous spheres, featuring highly dispersed molybdenum species and synthesized via the Stöber method, have demonstrated significant efficacy in removing 4, 6-DMDBT. Similarly, MoO_x@CN catalysts, anchored on nitrogen-doped carbon nets and prepared through a one-step pyrolysis technique, exhibit high efficiency in oxidative desulfurization using H₂O₂ (Ye et al., 2020). However, the above ODS processes are integrated with extraction steps that utilize polar solvents such as acetonitrile (Guo et al., 2023b), methanol (Luo et al., 2014), and dimethylformamide (DMF) (Julião et al., 2019), which increase operational complexity and environmental impact. The integration of reaction and separation into a single-step, solvent-free system could significantly improve the sustainability and efficiency of the ODS process. Therefore, the development of a dual-functional catalytic-adsorption system capable of operating in a solvent-free ODS environment is of paramount importance.

Porous materials, characterized by their tunable pore channels and morphologies, have demonstrated exceptional versatility in applications such as catalysis, separation, and adsorption applications (Chen et al., 2020; F. Li et al., 2022; Yang et al., 2021; Zhang et al., 2022). For instance, the catalyst Mo/mSiO₂, utilizing a 3D network of mesoporous SiO₂ nanowires as a support, demonstrates excellent adsorption of reaction products in ODS. This is attributed to the enhanced dispersion of Mo species and the increased surface area provided by the mesoporous SiO₂ framework, which facilitates efficient adsorption of reaction products (Dou and Zeng, 2014). Hollow SiO₂ (MoO_x/HS), which encapsulates MoO_x within hollow

structures, serve as a nanoreactor to prevent leaching of active components, thereby significantly improving the stability and catalytic activity of ODS. Notably, this design eliminates the requirement for extraction solvents, offering a more sustainable approach (Kuwahara et al., 2017). The amphiphilic nanoreactor Mo/ HNT/S, with MoO_x embedded in the internal HNT and its exterior surface modified with hexyltrimethoxysilane, has further streamlined the ODS process by integrating reaction and separation into a single step and eliminating the need for solvent extraction (Guo et al., 2023a). Despite these advancements, challenges remain in the selection of low-cost porous materials and the precise control of their surface polarity, which are critical for the development of efficient and scalable solvent-free ODS systems.

Biochar, recognized as a sustainable and cost-effective material, has demonstrated considerable potential in addressing environmental challenges, particularly in heterogeneous catalytic processes (Afshar and Mofatteh, 2024). Its distinctive properties, including a substantial surface area, high pore volume, and functional surface groups, make biochar a versatile material (Su et al., 2024). When integrated with other catalytic components, the performance of biochar in heterogeneous catalysis can be significantly enhanced (Brocza et al., 2024; Chen et al., 2024). Recent studies highlight the potential of biochar-based catalysts. For example, Song et al. (2024) crafted Cu-MOF-derived Cu nanoparticles adorned porous N-doped biochar for low-temperature H₂S desulfurization, while Yuan et al. (2023) employed MgFe₂O₄-loaded N-doped biochar, derived from waste cooked rice, for the same purpose. However, the removal of dibenzothiophene (DBT) from fuel oil remains a critical challenge. primarily due to difficulties in fine-tuning the surface polarity of biochar. Addressing this limitation could unlock the full potential of biochar as a promising candidate for ODS, thereby advancing its application in environmental technologies.

In this study, a series of novel dual-function amphiphilic biochar (Mo/CBC) catalysts, rich in oxygen vacancies, were successfully developed for efficient extractant-free oxidative desulfurization. The preparation process involved the activation of corn stalk biochar with KOH, followed by the introduction of MoO_{3-x} through an impregnation-calcination method, and subsequent carbonreduction to achieve amphiphilic properties. This innovative catalyst design ensures excellent dispersion and stability in oil, promotes efficient interaction with H₂O₂, and enables effective adsorption of sulfur-containing oxidation products. The Mo/CBC catalyst exhibited outstanding catalytic performance, achieving 99.6% desulfurization efficiency in 10 min without organic solvent extraction. The amphiphilic nature of the catalyst significantly reduces surface tension, prevents catalyst aggregation, and maximizes the utilization of active sites. Moreover, it enhances the adsorption of sulfurcontaining oxidation products, thereby streamlining the desulfurization process. The catalyst also demonstrated excellent recyclability, retaining full catalytic activity after five consecutive cycles, highlighting its durability and practical potential. This research presents a sustainable and efficient approach to fuel desulfurization, leveraging agricultural waste to develop dual-function catalysts. Beyond ODS, these catalysts hold significant promise for broader environmental applications, emphasizing their role in advancing sustainable catalytic technologies.

2. Materials and methods

2.1. Chemicals and reagents

Anhydrous ethanol was obtained from Tianjin Fuyu Fine Chemicals, benzothiophene (BT), dibenzothiophene, and 4,6-dimethyldibenzothiobenzene (4,6-DMDBT) were obtained from Macklin, and ammonium molybdate tetrahydrate

 $((NH_4)_6Mo_7O_{24}\cdot 4H_2O)$ was obtained from Aladdin. Corn stalk (Heilongjiang, China) served as the raw material to prepare raw biochar biomass, and then crushed and screened to obtain particles with a particle size of <1 mm. Rice straw, bamboo, rapeseed oil cake, and walnut oil cake were collected from Guizhou, and treated like corn stalk. All biomass materials are dried at 80 °C for 24 h before being prepared into biochar. All the chemicals were used without undergoing any purification procedures.

2.2. Preparation of catalysts

The preparation process of XMo/CBC_Y catalysts is depicted in Fig. 1(a). The specific preparation process of KOH activated corn stalk biochar (CBC_Y) is as follows. The corn stalk (20 g) was dried at 80 °C for 24 h to remove moisture. Then 5 g of dried corn stalk was pyrolyzed at 500 °C for 2 h under a N_2 atmosphere (heating rate of 5 °C/min). The resulting biochar was mixed with an aqueous solution of potassium hydroxide (KOH) at a mass ratio (KOH: biochar). The mixture was stirred (shaken at 120 rpm) at 100 °C until a black jelly-like slurry was formed, which was then transferred to a corundum boat crucible and heated to 700 °C in an N_2 atmosphere for 2 h. The activated product was subjected to alternate washing with water and ethanol three times, until the filtrate reached a

neutral pH. The washed product was dried at 80 $^{\circ}$ C for 12 h and then ball milled. The obtained activated biochar was labeled as CBC_Y (where Y represents the mass ratio of KOH to biochar, with Y values of 0, 1, 2, 3 and 4).

The synthesis of XMo/CBC_Y catalyst involved dissolving 32 mg of $(NH_4)_6Mo_7O_24\cdot 4H_2O$ in 20 mL of deionized water. Then, 0.2 g of CBC_Y (particle sizes ranging from 48 to 75 μ m) was added to the solution and stirred at 25 °C for 24 h. The product was centrifuged and then dried in a vacuum oven at 80 °C. The dried catalyst was subjected to pyrolysis at 500 °C for 2 h under a N_2 atmosphere to activate the catalyst. Different amounts of $(NH_4)_6Mo_7O_24\cdot 4H_2O$ were used in the synthesis, resulting in catalysts labeled as XMo/CBC_Y (where X=1, 2, 3, 4, 5, 6, with corresponding amounts of $(NH_4)_6Mo_7O_24\cdot 4H_2O$ being 16, 32, 64, 96, 128, and 160 mg, respectively). Other Mo-based catalysts from various biomass sources, including rice stalk biochar (Mo/SBC), bamboo biochar (Mo/BBC), rapeseed oil cake biochar (Mo/RBC), and walnut oil cake biochar (Mo/RBC) were prepared by using same method.

2.3. Catalytic ODS reaction

To assess the desulfurization ability of the catalyst, 432 mg of DBT was dissolved in 250 mL of *n*-octane to prepare a model fuel

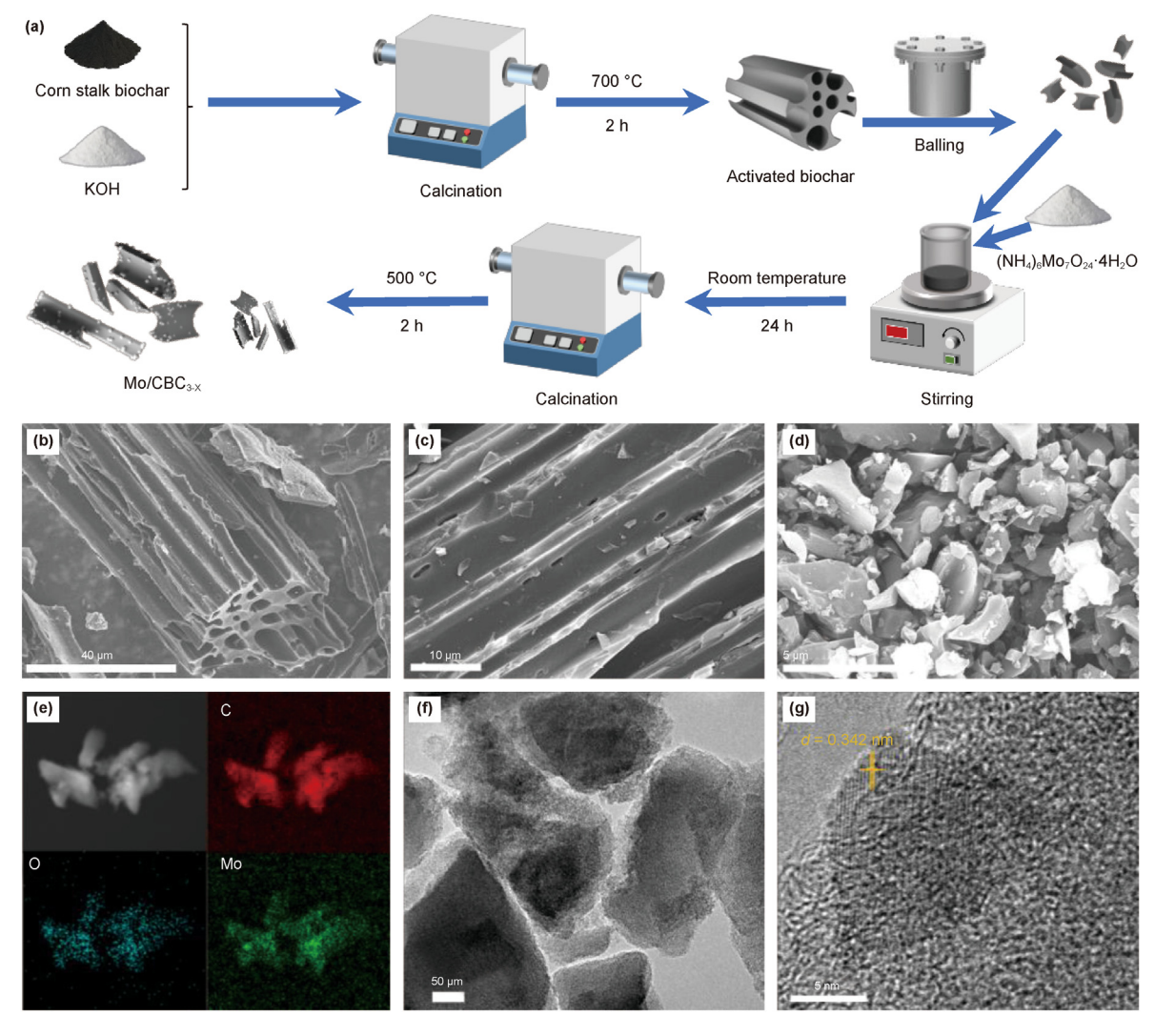


Fig. 1. (a) Schematic diagram of Mo/CBC₂ catalyst synthesis, SEM images of (b) CBC, (c) CBC₂ and (d) CBC₂ (after ball milling), (e) EDS mapping of 5Mo/CBC₂, (f) and (g) TEM images of 5Mo/CBC₂.

with a sulfur content of 300 ppm. The ODS experiments were conducted at $60\,^{\circ}$ C. Generally, $50\,\text{mg}$ of catalyst was added to $10\,\text{mL}$ of model fuel, followed by a specific amount of H_2O_2 solution. Clean oil was obtained by centrifuging the solid catalyst from the mixed solution, which was sampled every $5\,\text{min}$. The sulfur content of the treated oil was measured using a WK-2D microcoulometric detector. The efficiency of S-compound removal was calculated using the following formula.

$$\eta = (C_0 - C)/C_0 \times 100\%$$

The initial and final concentration of sulfur compounds are represented by C_0 and C, respectively, while the conversion rate of sulfur compounds is represented by η . After the reaction, the sulfide adsorbed by the catalyst was extracted using acetonitrile. The regenerated catalyst was then filtered, washed, and dried at 100 °C in preparation for the recovery experiment.

2.4. Characterizations

The Supporting Information provides detailed descriptions of the methods used for characterization in this study.

3. Results and discussion

3.1. Characterization of catalysts

The synthesis of a novel amphiphilic biochar (Mo/CBC) catalyst, enriched with MoO $_{3-x}$, was accomplished through a simple yet innovative approach, as illustrated schematically in Fig. 1(a). The process began with the activation of low-polarity corn stalk biochar using potassium hydroxide (KOH), followed by the incorporation of MoO $_{3-x}$ through an impregnation-calcination procedure. To further enhance the catalyst's properties, the biochar was subjected to ball milling, reducing particle size and facilitating the uniform loading of MoO $_{3-x}$ onto the biochar surface. The final amphiphilic Mo/CBC catalyst was obtained via the carbon reduction of molybdenum species, ensuring the formation of oxygen vacancies critical for its catalytic performance.

The morphology of the synthesized amphiphilic biochar (Mo/ CBC) MoO_{3-x} catalyst was examined using SEM and TEM, with the findings illustrated in Fig. 1. As shown in Fig. 1(b), the original corn stalk biochar exhibits a fibrous lignocellulosic structure. After KOH activation, the CBC₂ surface features fibrous tubes with numerous cracks (Fig. 1(c)), indicative pore formation due to pyrolysis and KOH activation (Lu et al., 2020; Nascimento et al., 2022). The ultimate analysis of biochar before and after activation, summarized in Table S1, shows an increase in the O/C ratio post-activation, correlating with enhanced surface hydrophilicity (Ullah et al., 2022). This increase in oxygen content enhances the biochar's polarity (Dissanayake et al., 2020), which gives it amphiphilic properties and makes it more suitable for extractant-free oxidation desulfurization. As depicted in Fig. 1(d) and S1, ball milling eliminated the tubular structure of CBC2, reducing particle sizes to 2-5 μm. The amorphous region created during ball milling augments surface energy (Zhao et al., 2022), facilitating MoO_{3-x} adsorption and dispersion.

Upon introducing Mo species, the morphology of 5Mo/CBC_2 particles has no significant change compared to CBC_2 (Fig. S2). Elemental mapping images (Fig. 1(e) and S3) verified the uniform distribution of Mo species on the CBC_2 surface. Additionally, no obvious large metal oxide particles were observed in the TEM image (Fig. 1(f)), indicating that MoO_{3-x} has good dispersibility on the biochar carrier (Liang et al., 2023). The lattice fringes with a spacing of 0.342 nm correspond to the (-111) plane of the MoO_{3-x} phase

within the nanoparticles (Fig. 1(g)) (Guo et al., 2023b; Yang et al., 2018). Collectively, the SEM and TEM analyses confirm the successful incorporation and uniform dispersion of Mo species on the CBC₂ surface, which is critical for its catalytic performance.

To delve deeper into the chemical structure, FT-IR and XRD analyses were performed. Fig. 2(a) displays the FT-IR spectra of CBC₂ and Mo/CBC₂. The CBC₂ spectrum features peaks at 849 and 3450 cm⁻¹, attributable to the C-H bond and the -OH group, respectively, formed during corn stalk carbonization and activation processes by KOH (Feng et al., 2023; Lu et al., 2020; Zhang et al., 2023). For Mo/CBC₂ samples with varying Mo contents, the FT-IR spectra of those with higher Mo contents (4Mo/CBC₂, 5Mo/CBC₂, and 6Mo/CBC₂) exhibit distinct new peaks at 928 and 869 cm⁻¹ corresponding to Mo=O and O-Mo-O vibrations, respectively, indicating the presence of MoO_{3-x} in the composites (Guo et al., 2023a). X-ray diffraction (XRD) patterns confirmed the presence of MoO₂ phase in high Mo content biochar catalysts (Fig. 2(b)). Due to the high dispersion of MoO_{3-x} on biochar, neither the characteristic peaks of MoO₂ nor MoO₃ can be observed in biochar catalysts with low Mo content. The diffraction peaks at 26.03° and 37.03° are consistent with the (-111) and (-211) facets of MoO₂ (JCPDS No. 32-0671). The results indicate that as the Mo content increases, the formation of a significant MoO2 phase becomes evident in the MoO_{3-x}/CBC_2 catalysts, highlighting the structural transformation with increasing Mo incorporation.

Electron paramagnetic resonance (EPR) was used to investigate the effect of biochar support and calcination atmosphere on oxygen vacancy content (Fig. 2(c)). In general, the symmetric signals (g=2.003) in EPR spectra correlate with the oxygen vacancy concentration (Di et al., 2021). Based on the previous XRD results (Fig. 2(b)), it is inferred that the molybdenum oxide phase in the catalysts is not purely MoO₃ or MoO₂, but rather MoO_{3-x}, characterized by the presence of oxygen vacancies. Notably, the EPR signal intensity of 5Mo/CBC_2 (Fig. 2(c)) was the strongest, indicating a higher density of oxygen vacancies compared to MoO_{3-x} synthesized without a biochar support and calcined under air or nitrogen atmosphere, respectively. This enhancement can be attributed to the carbon-mediated reduction of MoO_3 at the biochar interface, which promotes the formation of oxygen vacancies in 5Mo/CBC_2 catalysts (Guo et al., 2023b).

To further validate the pivotal role of carbon reduction during the formation of MoO_{3-x} on biochar, in-situ thermal XRD testing was conducted (Fig. 2(d)). The results provide direct evidence supporting the carbon-biochar interface as a key factor in the generation of oxygen vacancies and the stabilization of MoO_{3-x} phases under controlled calcination conditions. In the preparation of catalyst 5Mo/CBC2, the reduction of Mo by biochar occurred in three distinct stages. (1) (NH₄)₆Mo₇O₂₄·4H₂O remained undecomposed at 200 °C, with diffraction peaks at 12.38°, 17.44°, 19.89°, and 33.95° corresponding to its (-121), (061), (-142), and (271) facets, respectively (JCPDS No. 27-1013). (2) Upon calcination at 200-350 °C, (NH₄)₆Mo₇O₂₄·4H₂O began to decompose and form MoO₃. The peaks located at 12.77°, 23.33°, 25.70°, and 27.33° corresponded to the (020), (110), (040), and (021) facets of MoO₃ (JCPDS No. 05–0508). (3) As the temperature increased, MoO_3 was reduced to MoO₂ by the biochar, and the XRD pattern of 5Mo/CBC₂ showed the main phase of MoO₂ (JCPDS No. 32–0671). The peaks at 18.45°, 26.03°, 31.78°, 37.03°, 41.36° that respectively conform to the MoO₂ crystal facet of (-101), (-111), (101), (-211) were clearly observed. However, the MoO_{3-x} (500 $^{\circ}$ C/N₂) and MoO_{3-x} (500 $^{\circ}$ C/ Air) diffraction peaks were located at 12.77°, 23.33°, 25.70°, and 27.33°, corresponding to the (020), (110), (040), and (021) facets of MoO₃ (JCPDS No. 05–0508) (Fig. S4). These results confirm that molybdenum oxide undergoes reduction with biochar at conditions above 400 °C, leading to the formation of oxygen vacancies. To

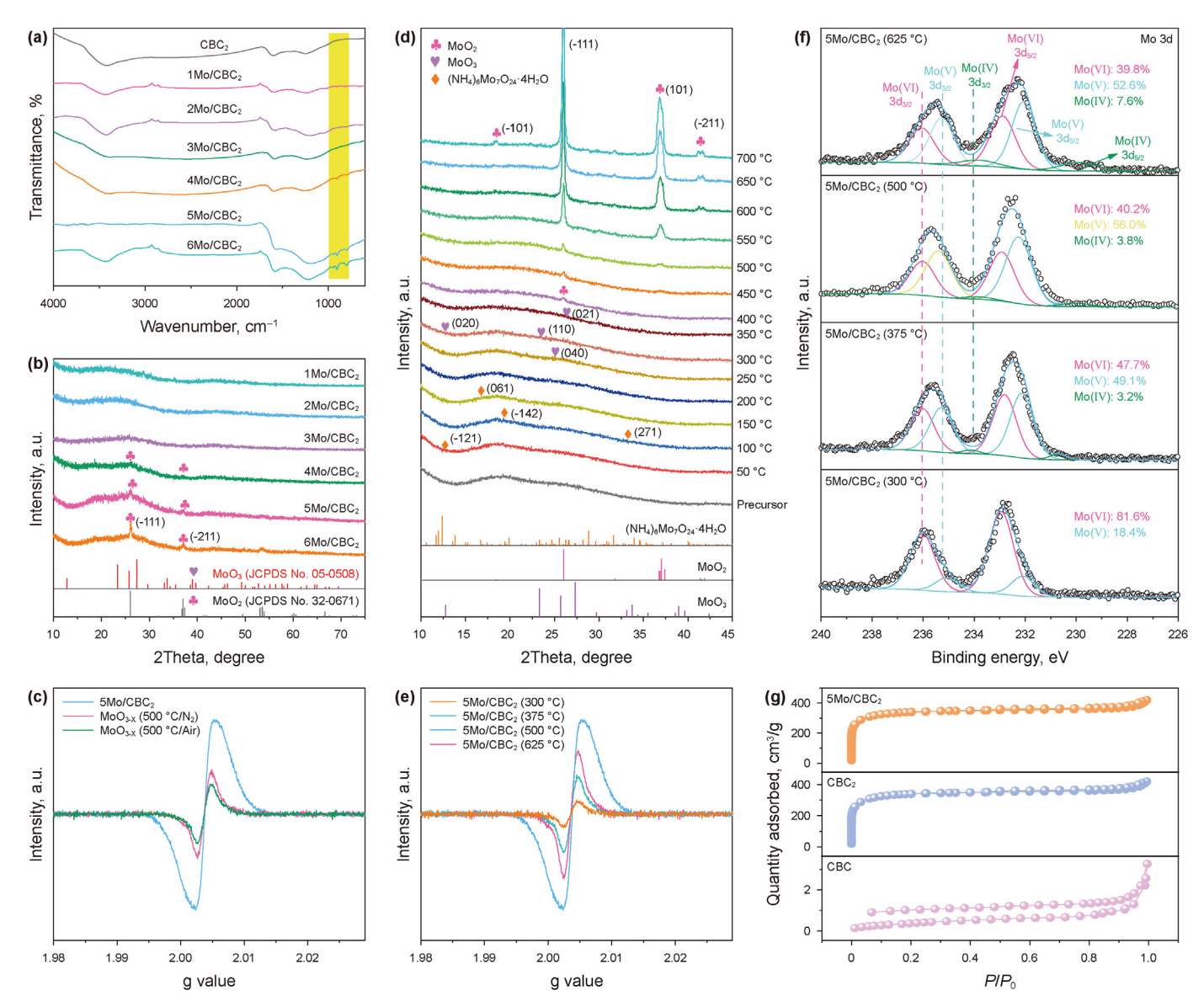


Fig. 2. (a) FT-IR spectra of CBC₂ and XMo/CBC₂; (b) XRD patterns of XMo/CBC₂; (c) EPR spectra of MoO_{3-x} (500 °C/N₂), MoO_{3-x} (500 °C/Air), and 5Mo/CBC₂, (MoO_{3-x} (500 °C/Air): sample obtained by calcination of ammonium molybdate at 500 °C in air, MoO_{3-x} (500 °C/N₂): sample obtained by calcination of ammonium molybdate at 500 °C in N₂; (d) In-situ XRD patterns of 5Mo/CBC₂ precursor calcined at different temperatures; (e) EPR spectra of 5Mo/CBC₂ precursor at different calcination temperature (temperature represents the calcination temperature of 5Mo/CBC₂ precursor.); (f) Core-level Mo 3d peaks obtained from the XPS analysis of 5Mo/CBC₂ precursor at different calcination temperatures; (g) N₂ adsorption desorption isotherms of CBC, CBC₂, and 5Mo/CBC₂.

further investigate how oxygen vacancies vary with calcination temperature, EPR tests were performed on 5Mo/CBC_2 catalyst. The EPR spectra of 5Mo/CBC_2 calcined at different temperatures are shown in Fig. 2(e). As the calcination temperature of the 5Mo/CBC_2 precursor increases, the amount of oxygen vacancies first increases and then decreases. This process involves the decomposition of $(NH_4)_6\text{Mo}_7\text{O}_{24}$ to form MoO_3 firstly, and then as the temperature increases, the layered MoO_3 is reduced by biochar and fused between layers to form MoO_2 phase, resulting in an increase in oxygen vacancies.

As the temperature continues to rise, MoO₃ is excessively reduced, resulting in a decrease in oxygen vacancies. These results confirm that the oxygen vacancy concentration in 5Mo/CBC₂ can be tuned by adjusting the calcination temperature. XPS spectra was utilized to identify the Mo species on the MoO_{3-x}/CBC₂ prepared under different temperatures. Fig. 2(f) shows six fitted peaks in the Mo 3d spectrum at 235.9, 234.8, 233.1, 232.7, 231.8, and 229.8 eV,

assigned to Mo (VI) $3d_{3/2}$, Mo (V) $3d_{3/2}$, Mo (IV) $3d_{3/2}$, Mo (VI) $3d_{5/2}$, Mo (VI) $3d_{5/2}$, and Mo (IV) $3d_{5/2}$, respectively (An et al., 2024; Wang et al., 2023). As the calcination temperature increased from 300 to 625 °C, the proportion of Mo (V) on the MoO_{3-x} surface initially rose, then declined. Concurrently, the proportion of Mo (IV) on the MoO_{3-x} surface increased from 0 to 7.6%, with a tendency for the proportion of Mo (VI) to increase and then decrease. The reduction in Mo (V) content on the MoO_{3-x} surface with increasing calcination temperature is consistent with EPR spectra results (Fig. 2(e)). In situ XRD, EPR, and XPS spectra collectively suggest that biochar can reduce Mo (VI) species to generate oxygen vacancies, with the extent of vacancy formation being modulated by calcination temperature. Consequently, a novel MoO_{3-x}/CBC₂ catalyst with abundant oxygen vacancies was successfully synthesized.

Furthermore, the N_2 adsorption-desorption isotherms and pore size distribution curves of CBC, CBC₂, and 5Mo/CBC₂ are presented in Fig. 2(g) and Fig. S5. The biochar surface area after activation

surged from 2.24 to 1120.53 m $^2 \cdot g^{-1}$ (Table S1), underscoring the critical role of KOH chemical activation. Intriguingly, the specific surface area of MoO_{3-x}-modified biochar catalysts did not diminish significantly, particularly the pore volume. The pore size distribution curve analysis revealed that 5Mo/CBC₂ boasts an abundance of microporous/mesoporous structures ranging from 1 to 4 nm. This observation is corroborated by HRTEM image of 5Mo/CBC₂, which shows numerous micropores (Fig. 1(g)). The large molecular size of DBT (6.07 \times 9.81 Å) facilitates rapid mass transfer within these micro/mesoporous structures, enhancing the reaction rate by contacting active sites. In summary, KOH-activated biochar generates additional pores, exposing more accessible active sites for catalysis (Yang et al., 2020).

To further elucidate the formation process of oxygen vacancyrich MoO_{3-x} (O_{vac}-MoO₃) on biochar, the schematic of the partial carbon-reduction reaction of the MoO₃ layers (Fig. 3) was proposed based on the analysis results from EPR, in situ XRD, and XPS. As the carbon reduction temperature rises, the XRD peak corresponding to MoO₂ becomes more pronounced (Fig. 2(d)), indicating an increased presence of the MoO₂ phase. However, XPS data reveals the existence of Mo (VI) and Mo (V), with a relatively low amount of Mo (IV) at higher temperatures (Fig. 2(f)). These apparently contradictory findings suggest that the final Mo/CBC₂ sample contains MoO_{3-x} species alongside the MoO₂ structure. Given that XPS is adept at surface analysis while XRD probes deeper into samples, it is deduced that during the carbon reduction calcination process, MoO₃ layers undergo sintering to form MoO₂ while preserving a surface laver with the structural traits of MoO₃, including oxygen vacancies, created by carbon reduction, as depicted in Fig. 3. The reduction sintering of MoO₃ under hydrogen gas to produce MoO₂ has been validated by Zhang et al. (2017). The depletion of surface lattice oxygen (O^{2-}) in the few-layer MoO_3 leads to the formation of Mo (V) species during partial reduction. As the reduction time extends, the high concentration of exposed Mo (V) species catalyzes the re-bonding of Mo and O across different layers, resulting in the formation of MoO₂. Due to the lower reduction capability of carbon

or CO compared to H_2 , the surface of MoO_2 , generated from the reduction of MoO_3 , exhibits defect structures characteristic of MoO_3 , containing Mo (VI) and Mo (V). Consequently, as the reduction temperature increases, adjacent MoO_3 particles undergo sintering, driven by the carbon reduction process. This phenomenon is supported by BET data (Table S1), which indicate particle growth and a reduction in surface area. The sintering of MoO_{3-x} particles leads to a decline in the number of accessible active sites featuring oxygen vacancies, thereby correlating with a notable decrease in desulfurization efficiency.

3.2. Assessment of oxidative desulfurization efficiency

The DBT removal efficiencies of carrier and XMo/CBC₂ samples with different Mo loading (2%–12%) were investigated in Fig. 4(a). The desulfurization efficiency of the carrier (CBC₂) is only 14.32%, which can be attributed to the porous structure and abundant surface functional groups of the activated biochar, allowing it to adsorb DBT (Yang et al., 2018). The 5Mo/CBC₂ sample, containing 9.92 wt% Mo, demonstrates superior catalytic performance compared to 1Mo/CBC₂ with the Mo content of 2.16 wt% (Table S2). As the Mo content increases, the desulfurization efficiency of XMo/ CBC2 catalyst also rises. The amphiphilic 5Mo/CBC2 catalyst displayed exceptional catalytic performance in ODS, achieving a desulfurization efficiency of 99.6% in merely 10 min without using extraction solvent. However, the performance of 6Mo/CBC₂, with 11.75 wt% Mo, declines, likely due to the excessive aggregation of MoO_{3-x} (Rajendran et al., 2022; Yang et al., 2009). Reaction kinetics, detailed in Table S2, reveal that the ODS system conforms well to pseudo-first-order kinetics. The desulfurization rates for catalysts with different Mo contents are 0.014, 0.14, 0.18, 0.26, 0.34, and 0.22 min⁻¹, respectively (Fig. 4(b)). This indicates that the optimal amount of MoO_{3-x} on the biochar surface is crucial for achieving superior catalytic performance. Excessive Mo loading leads to aggregation, reducing the accessibility of active sites and thereby compromising the catalyst's efficiency.

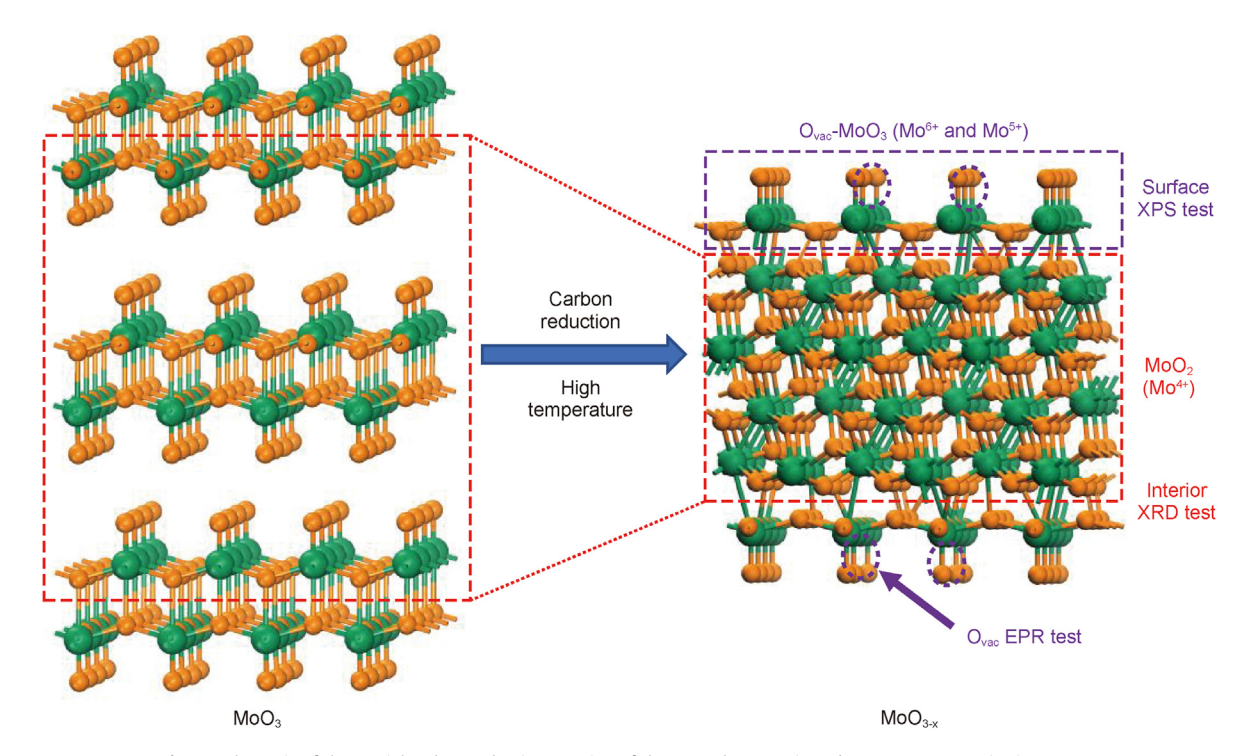


Fig. 3. Schematic of the partial carbon-reduction reaction of the MoO₃ layers to introduce oxygen vacancies in MoO_{3-x}.

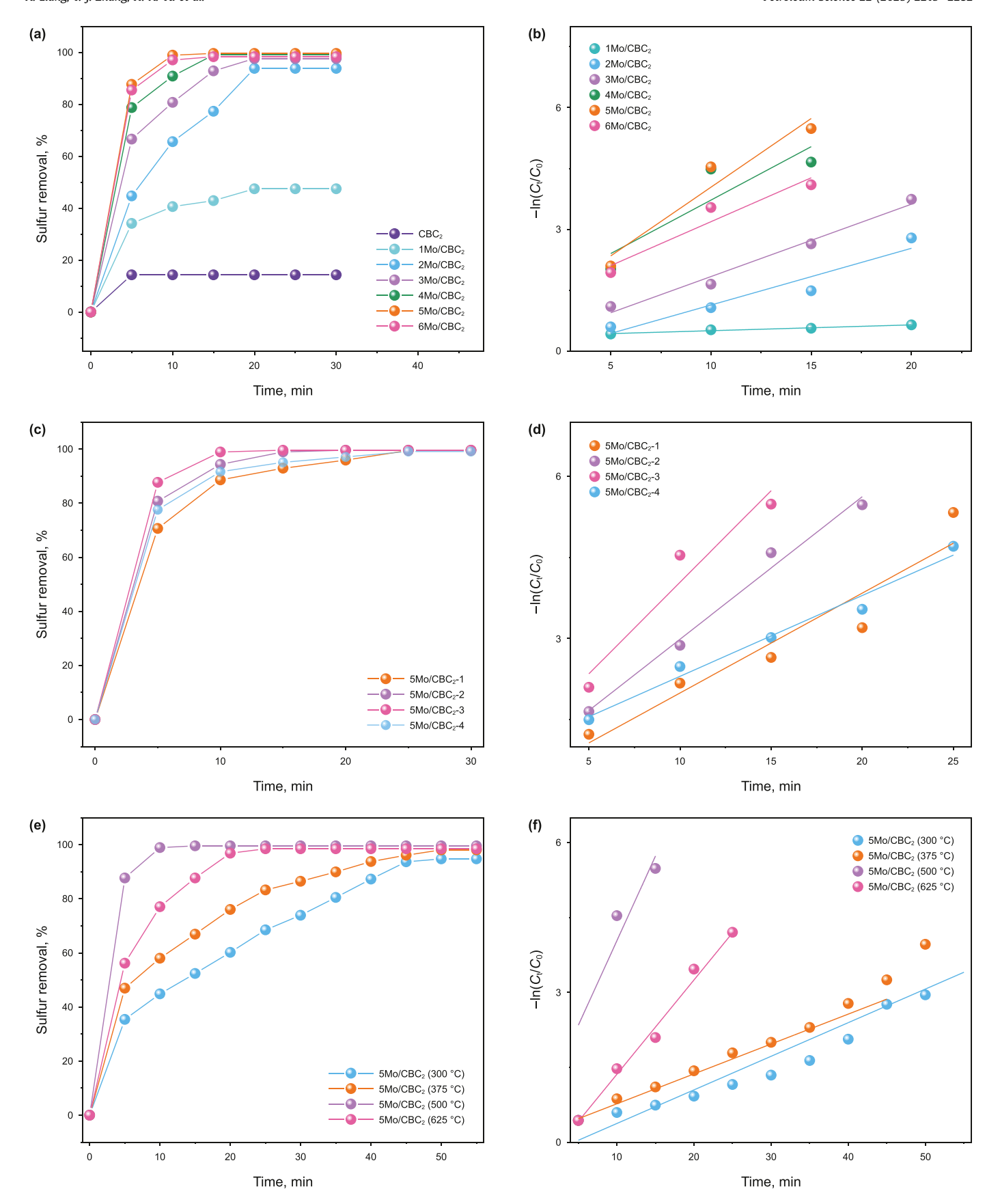


Fig. 4. (a) Carrier and catalytic performance and (b) experimental data were fitted to a first-order kinetic model of XMO/CBC_2 , (c) catalytic performance and (d) experimental data were fitted to a first-order kinetic model of $5MO/CBC_2$ with different biochar particle sizes prepared by ball milling, (e) catalytic performance and (f) experimental data were fitted to a first-order kinetic model of the different calcination temperature. Reaction conditions: $m_{\text{catal}} = 50 \text{ mg}$, $V_{\text{oil}} = 10 \text{ mL}$, initial S-content = 300 ppm, O/S = 6, $T = 60 \, ^{\circ}\text{C}$.

Apart from the Mo content of biochar catalyst, the particle size of CBC2 controlled by ball milling also plays a crucial role in determining the Mo content of the catalyst. As shown in Table S3, 5Mo/CBC₂-1 to 5Mo/CBC₂-4 represent the particle size of >150 μ m, 74-150 μm, 48-74 μm and 34-48 μm, respectively. A progressive decrease in particle size results in a consistent increase in Mo content, even when the ammonium molybdate concentration remains unchanged. This is attributed to the higher surface energy and increased amorphous regions generated during the ball milling process (Zhao et al., 2022), which promote Mo loading. Notably, larger particle sizes, such as those of 5Mo/CBC₂-1, result in underutilization of both internal and external surfaces of the carrier, lower loading of catalytic active centers, and consequently lower desulfurization efficiency (Fig. 4(c) and (d)). As the particle size decreases, the Mo content in 5Mo/CBC2-2 is 9.14%, and the adsorption efficiency reaches 97.97% (Fig. 4(c)). The kinetic simulation of the relevant catalysts conforms to the quasi first order kinetics, with k being 0.25 min⁻¹ (Fig. 4(d)). The 5Mo/CBC₂-4 catalyst, with the smallest particle size, exhibits more exposed groups and regions, leading to a Mo content of 11.03%. However, the increased number of Mo content leads to its agglomeration, resulting in decreased desulfurization efficiency. Moreover, by reducing carrier particle size through ball milling, the contact path between active sites and catalytic substrate is shortened, accelerating the reaction rate. The 5Mo/CBC₂-3 (later abbreviated as 5Mo/ CBC₂) sample was selected for further catalytic experiments due to its optimal balance of high Mo content and superior desulfurization efficiency.

The above EPR, in situ XRD, and XPS characterizations confirm that the calcination temperature has an impact on the content of oxygen vacancies in the catalyst. Therefore, the effect of calcination temperature of 5Mo/CBC₂ catalyst on its desulfurization efficiency was studied. As shown in Fig. 4(e), the desulfurization efficiencies of 5Mo/CBC₂ at different calcination temperatures (300 °C), 5Mo/ CBC₂ (375 °C), 5Mo/CBC₂ (500 °C), and 5Mo/CBC₂ (625 °C) are 92.5%, 94.7%, 99.6%, and 98.1%, respectively. The catalytic performance of the catalysts follows the order of measured reaction rate constants: 5Mo/CBC_2 (500 °C) (0.34 min⁻¹) > 5Mo/CBC_2 (625 °C) $(0.19 \text{ min}^{-1}) > 5\text{Mo/CBC}_2 (375 ^{\circ}\text{C}) (0.060 \text{ min}^{-1}) > 5\text{Mo/CBC}_2$ $(300 \,^{\circ}\text{C}) \, (0.058 \, \text{min}^{-1}) \, (\text{Fig. 4(f)} \, \text{and Table 1})$. A correlation analysis between surface Mo species proportions and desulfurization rate indicated of biochar-MoO_{3-x} catalysts that Mo (V) showed a strong positive correlation with desulfurization rate, while Mo (IV) and Mo (VI) are negatively correlated. The presence of surface Mo (V) species in biochar-MoO_{3-x} catalyst plays a critical role in accelerating the desulfurization rate, underscoring its importance in achieving superior catalytic efficiency.

To achieve the optimal removal efficiency of DBT on 5Mo/CBC_2 catalyst, the effect of reaction conditions including catalyst weight, $\text{H}_2\text{O}_2/\text{DBT}$ molar ratio (denoted O/S), and reaction temperature were studied. The catalytic activity of 5Mo/CBC_2 catalyst was investigated by varying catalyst amount from 20 to 50 mg (Fig. 5(a)). Generally, a larger catalyst amount provides more active sites, leading to higher desulfurization efficiency. The desulfurization efficiency of 5Mo/CBC_2 catalyst increased as the amount of catalyst increased and the desulfurization rate reach 99.6% for

Table 1Kinetic parameters of catalytic oxidation desulfurization reaction.

Sample	<i>k</i> , min ⁻¹	R^2		
5Mo/CBC ₂ (300 °C)	0.0577	0.9404		
5Mo/CBC ₂ (375 °C)	0.0599	0.9832		
5Mo/CBC ₂ (500 °C)	0.3387	0.9689		
5Mo/CBC ₂ (625 °C)	0.0673	0.9237		

10 min was observed at a catalyst dosage of 50 mg. By increasing the amount of catalyst to 60 mg, DBT removal did not become significantly faster. Therefore, the optimal catalyst usage is chosen as 50 mg. In the ODS system, the dosage of oxidant is a key factor influencing DBT removal. At an O/S (H_2O_2/DBT) molar ratio of 2, the DBT removal rate was only 68.67% due to insufficient H_2O_2 . With increasing the O/S molar ratio to 6, the DBT removal rate of 5Mo/CBC₂ catalyst reached 99.6% within 10 min (Fig. 5(b)).

The removal rate of DBT initially increased and then decreased with increasing H_2O_2 content due to the decomposition of excess H_2O_2 (O/S = 8), leading to an increase in interfacial mass transfer resistance and a decrease in mass transfer rate (Y. Liu et al., 2021). Therefore, the O/S molar ratio was set to 6 in the subsequent experiments. Achieving mild reaction conditions and high desulfurization efficiency are crucial for fuel desulfurization in real industry (Liu et al., 2023). As an endothermic reaction, higher temperatures promote the ODS process. The catalytic rate increased with temperature at 40, 50, and 60 °C (Fig. 5(c)). However, further increasing the temperature to 70 °C led to a decrease in desulfurization efficiency, which is attributed to the decomposition of H_2O_2 at elevated temperatures, reducing the effective utilization of oxidants in the ODS process.

The reaction kinetics, detailed in Table S4, follow pseudo-first-order kinetics, providing insight into the DBT oxidation reaction. The non-spontaneous nature of the catalytic oxidation of DBT is evident from the positive ΔH values (Table S5), suggesting that the process absorbs heat and that slightly higher temperatures are beneficial for enhancing the DBT reaction. Considering both the desulfurization rate and economic factors (Fig. 5(d)), 60 °C was determined to be the optimal reaction temperature, balancing efficiency and operational costs in practical applications.

In order to further investigate the effect of catalyst polarity on its oxidative desulfurization performance, the desulfurization performance, water contact angle, and dispersibility in oil and water phases of biochar catalysts activated with varying amounts of KOH. In multiphase reaction systems, particularly in extractant-free catalytic oxidation desulfurization, the immiscibility and high interfacial tension between oil and water create challenges for dispersing the limited amount of $\rm H_2O_2$ within the oil phase. Industrial reactors are often ineffective for this heterogeneous ODS process.

KOH activation increases the oxygen content of biochar, enhancing both its surface area and hydrophilicity (Rajapaksha et al., 2016). Table S1 shows the O/C atomic ratios of biochar and its derivatives. Activation of biochars with KOH has reduced C% and increased O%. The O/C of 5Mo/CBC₂ sample calcined at 500 °C, a decrease in the O/C ratio is observed, indicating that oxygen within the biochar structure is consumed at elevated temperatures.

At 300 °C, the O/C of 5Mo/CBC₂ is higher than that of the 5Mo/CBC₂ calcined at 500 °C, indicating a decreasing trend in O/C with increasing calcination temperature. A higher O/C ratio also implies increased hydrophilicity (Ahmad et al., 2012; Dissanayake et al., 2020). Without KOH treatment, the DBT removal rate of 5Mo/CBC₀ was only 16.3% (Fig. 6(a)), which is attributed to the strong hydrophobicity of the catalyst, which hinders contact with the oxidant. On the other hand, the smaller specific surface area of 5Mo/CBC₀ prevents the dispersion of Mo species, resulting in a lower Mo content (Table 2) and reduced catalytic activity. By modifying biochar with KOH, both the catalyst's polarity and pore structure are significantly improved. KOH activation increases the specific surface area (Table S1), thereby enhancing Mo species dispersion and improving oxidative desulfurization performance.

When KOH/CBC = 1, the DBT removal rate of catalyst (5Mo/CBC₁) reached 71.0% (Fig. 6(a) and (b)). Although this catalyst showed improved desulfurization efficiency compared to 5Mo/

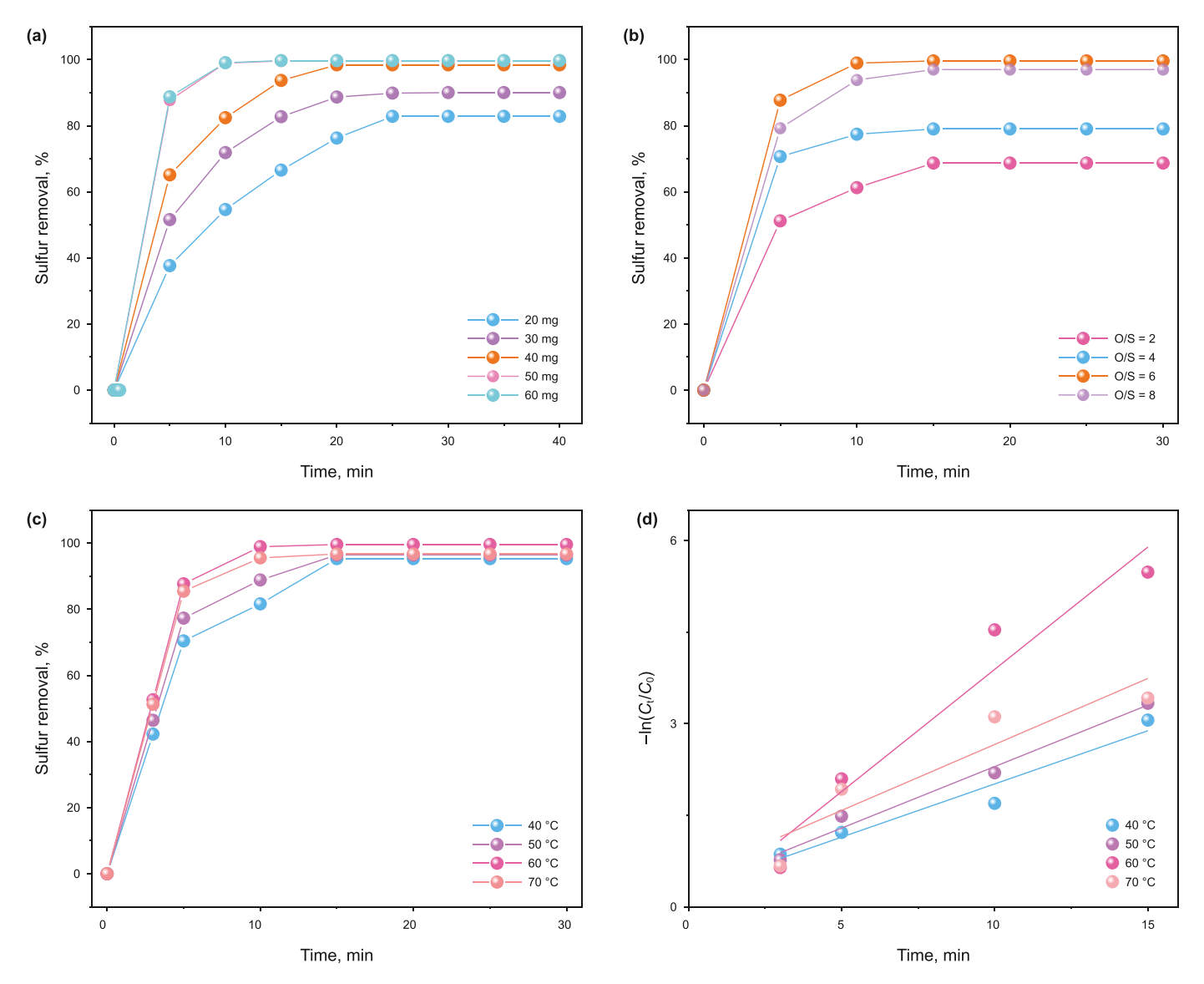


Fig. 5. Effect of reaction conditions on DBT conversion of 5Mo/CBC₂ catalyst: (a) catalyst amount, (b) O/S, (c) reaction temperature, and (d) fitting of reaction temperature experimental data to pseudo-first-order kinetic mode. Reaction conditions unless above mention: $m_{\text{catal}} = 50 \text{ mg}$, $V_{\text{oil}} = 10 \text{ mL}$, initial S-content = 300 ppm, O/S = 6, $T = 60 \, ^{\circ}\text{C}$.

 CBC_0 , it still does not meet the national sulfur standards for fuel oil. This limitation arises from the catalyst's low hydrophilicity, creating interfacial resistance with H2O2 that hinders DBT oxidation. To explore this further, water contact angle experiments and dispersibility experiments in oil and water phases were conducted to investigate the amphiphilicity of 5Mo/CBCY catalysts (Fig. 6(c), Figs. S6 and S7). The contact angle of 5Mo/CBC₀ (92.7°) is larger than that of 5Mo/CBC₁ (77.9°), indicating KOH can enhance their hydrophilicity. This result has also been confirmed by oil-water dispersibility experiments (Fig. 6(c)). At KOH/CBC = 2, the biochar catalyst (5Mo/CBC₂) exhibits amphiphilicity with a maximum desulfurization efficiency of 99.6% within 10 min. The reaction kinetics, illustrated in Fig. 6(b), follow pseudo-first-order kinetics, and the reaction rate constants for DBT oxidation were highest for 5Mo/CBC₂ among catalysts with different KOH contents. The intermediate contact angle of 5Mo/CBC2 (64.2°) indicates amphiphilicity (Fig. S8), allowing it to disperse in both aqueous and oil phases. Continuing to increase the mass of KOH, the desulfurization efficiencies of 5Mo/CBC₃ and 5Mo/CBC₄ present a downward trend, and are 68.7% and 47.5%, respectively, consistent with the catalysts'

increased polarity. Higher KOH ratios reduced the water contact angle (WCA) (Fig. 6(c), Figs. S9 and S10), and as polarity increased, the catalysts initially dispersed in water preferentially, then exhibited amphiphilic behavior, and eventually became hydrophilic, dispersing only in water (Fig. 6(c)). The above results confirm that the polarity of the biochar catalyst can be adjusted by the amount of KOH. With an optimal KOH amount, an amphiphilic biochar catalyst is produced, achieving the highest catalytic oxidation desulfurization performance.

In addition, it was found that the polarity of the biochar also affects the loading amount of Mo. Except for $5\text{Mo}/\text{CBC}_0$, there was minimal variation in Mo content among the other catalysts (Table 2), suggesting that the suitable polarity and large specific surface area and abundant micro/mesoporous structure contributed to $\text{MoO}_{3\text{-x}}$ loading. Interestingly, the difference in catalytic performance of $5\text{Mo}/\text{CBC}_Y$ is not related to Mo content, and the above results confirm that this is attributed to the polarity of the catalyst (Fig. 6(c)). The enhancement of catalyst activity was primarily due to the increased active sites at the catalyst interface. The amphiphilicity of the catalyst facilitated better dispersion of the

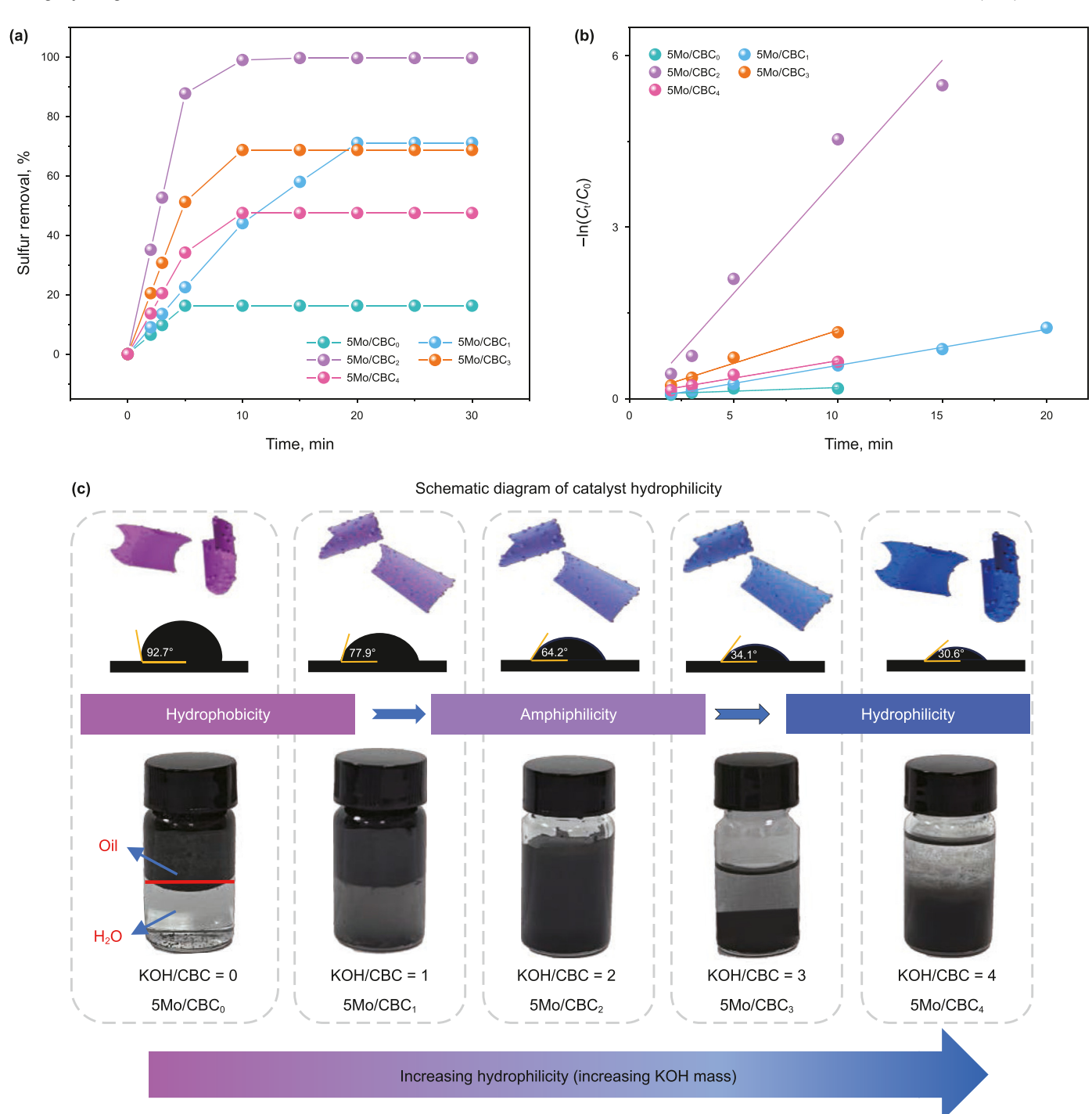


Fig. 6. (a) Catalytic performance of $5\text{Mo}/\text{CBC}_Y$, (b) the experimental data were fitted to a first-order kinetic model. Reaction conditions: $m_{\text{catal}} = 50 \text{ mg}$, $V_{\text{oil}} = 10 \text{ mL}$, initial Scontent = 300 ppm, O/S = 6, $T = 60 ^{\circ}\text{C}$. (c) The water contact angle diagrams of catalysts ($5\text{Mo}/\text{CBC}_Y$) with different polarities obtained by controlling the amount of potassium hydroxide, as well as their dispersion in oil and water.

Table 2Actual molybdenum weight% according to ICP-OES analysis.

Mo (wt.), %
2.04
9.32
9.92
9.98
9.64

adsorbent within the oil/water reaction system, reduce the interfacial resistance between oil and water, and improve the removal efficiency of DBT. Based on the above analysis, this study successfully developed a controllable amphiphilic Mo/CBC catalyst for deep desulfurization of fuel oil. The catalyst design achieves a balance between hydrophilicity and hydrophobicity, maximizing catalytic oxidation efficiency.

To meet the actual expectations of ODS industry, the performance of the examined biochar catalyst must be tested at varied

thiophene compounds, because the organosulfur compounds are complex in real oils. As seen in Fig. 7(a), different aromatic sulfides (DBT, BT and 4, 6-DMDBT) were used as substrates to evaluate the ODS performance of the catalysts. The desulfurization efficiency of DBT reached 99.6% within 10 min, while that of 4, 6-DMDBT and BT reached 70.55% and 60.36%, respectively (Fig. 7(a)). The reactivity followed the order: DBT > 4. 6-DMDBT > BT. This difference in desulfurization efficiency can be attributed to the spatial hindrance and electron density of the sulfur atoms. The S electron density in DBT (5.758) and 4,6-DMDBT (5.760) was higher than that in BT (5.739) (Fig. S11) (Guo et al., 2023a; Ye et al., 2021). In the ODS process, higher S electron density favored catalytic reactions (McNamara et al., 2013). However, the steric hindrance from the two methyl groups on 4, 6-DMDBT resulted in lower desulfurization performance compared to DBT. These results demonstrate the broad applicability of the catalyst for treating various aromatic sulfides, highlighting its potential value for addressing the challenges of the ODS industry.

For comparison, ODS systems using TBHP and O₂ as oxidants were also investigated in 5Mo/CBC₂ catalyst (Fig. 7(b)). Substituting

 $\rm H_2O_2$ with TBHP resulted in a significant 16.6% reduction in DBT removal efficiency under the same conditions. However, as an oxidant, $\rm O_2$ exhibits a desulfurization efficiency of only 9.25% under the same conditions. Oxygen has weak oxidizing ability as an oxidant, so it cannot be used as an oxidant in this system. The active site $\rm MoO_{3-x}$ need to be oxidized by strong oxidants ($\rm H_2O_2$ or TBHP) to form an active intermediate state that can react with DBT (Liu et al., 2023). However, the tert-butanol converted from TBHP will also be adsorbed on $\rm 5Mo/CBC_2$ catalyst, covering the catalytic sites and ultimately leading to a decrease in ODS performance. These findings emphasize the critical role of selecting an appropriate oxidant to achieve optimal catalytic activity in ODS systems.

Industrial catalysts require not only high catalytic activity but also excellent reusability and stability. The stability of 5Mo/CBC₂ catalyst was evaluated through cyclic experiments (Fig. 7(c)). Notably, after five cycles of recycling, the sulfur removal capacity of the spent catalyst without washing with acetonitrile between runs decreased to only 36.62% (Fig. 7(c) red column). This is attributed to the surface adsorption of oxidized sulfur-containing compounds (DBTO₂) on 5Mo/CBC₂ catalyst. However, when the catalyst was

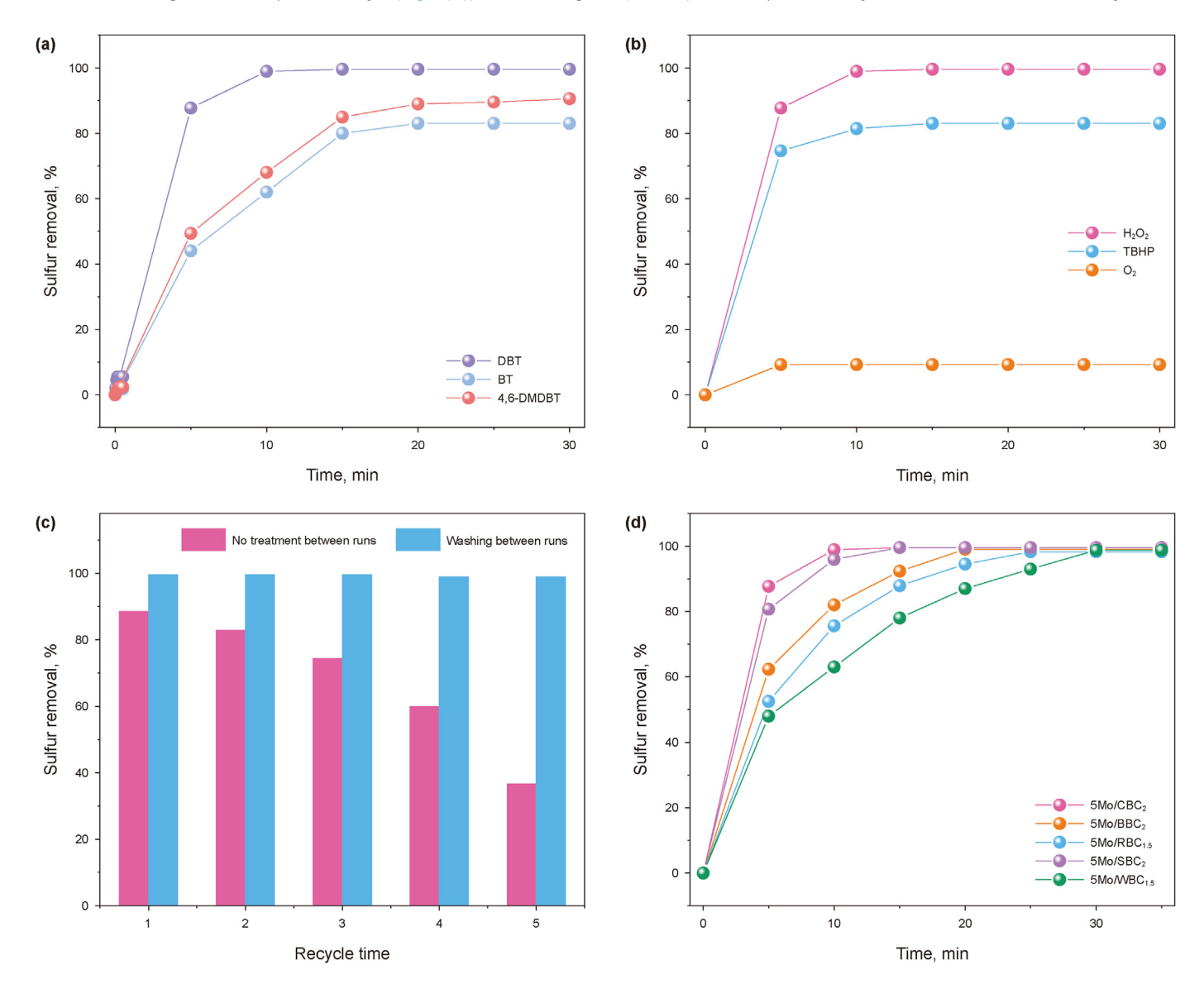


Fig. 7. Catalytic performance of **(a)** different sulfur-containing compounds and **(b)** different oxidants on $5\text{Mo}/\text{CBC}_2$ catalyst. **(c)** The recycling experiments of spent $5\text{Mo}/\text{CBC}_2$ catalyst with or without washing with acetonitrile between runs, **(d)** catalytic performance of $5\text{Mo}/\text{CBC}_2$, $5\text{Mo}/\text{BBC}_2$, $5\text{Mo}/\text{RBC}_{1.5}$, $5\text{Mo}/\text{SBC}_2$, and $5\text{Mo}/\text{WBC}_{1.5}$. Reaction conditions: $m_{\text{catal}} = 50 \text{ mg}$, $V_{\text{oil}} = 10 \text{ mL}$, initial S-content = 300 ppm, O/S = 6, $T = 60 \, ^{\circ}\text{C}$, t = 30 min.

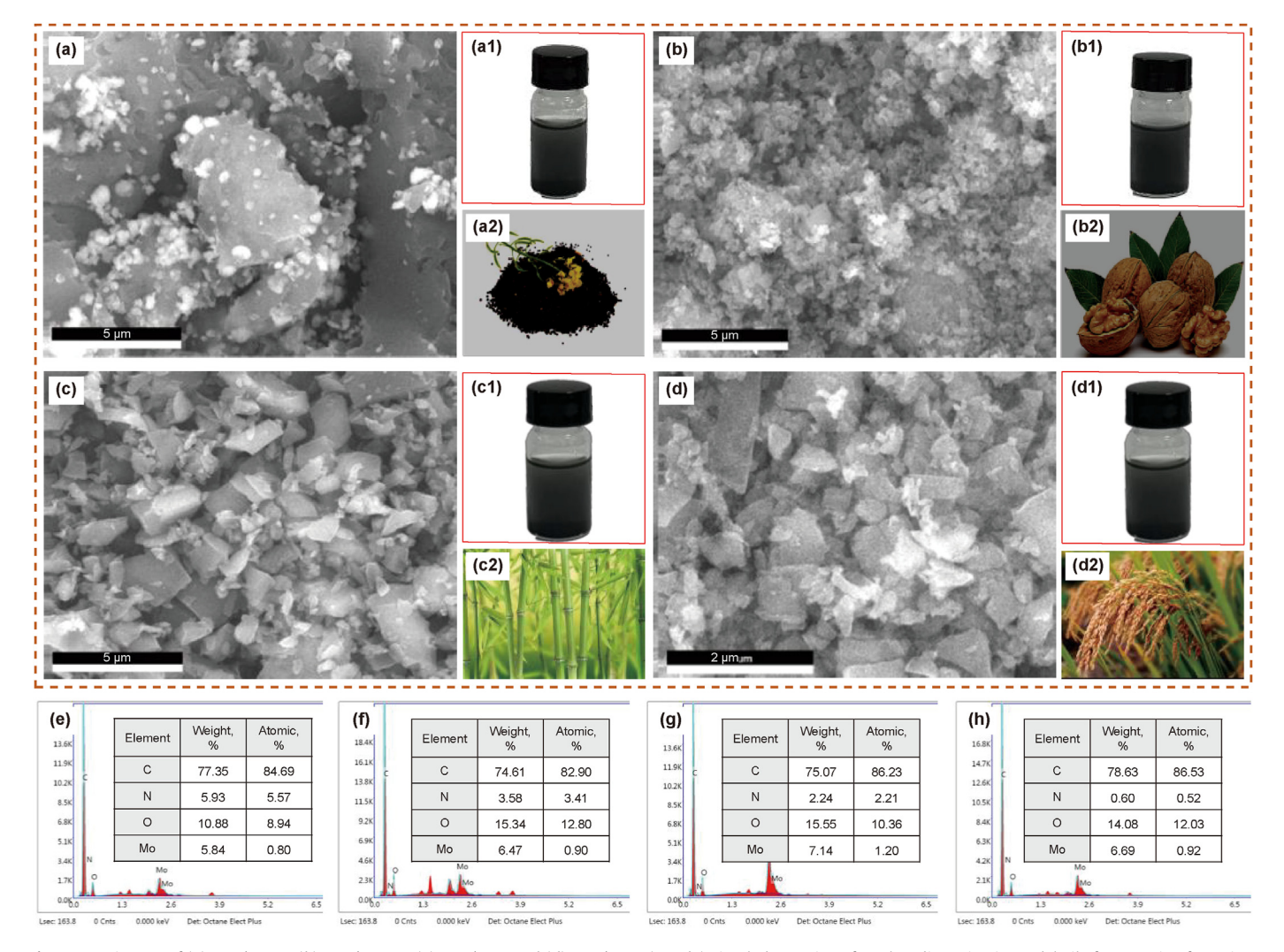


Fig. 8. SEM images of (a) 5Mo/RBC_{1.5}, (b) 5Mo/WBC_{1.5}, (c) 5Mo/BBC₂ and (d) 5Mo/SBC₂, (a1-d1) visual observation of catalyst dispersion in model oil after 30 min of reaction, photos of (a2) rapeseed, (b2) walnuts, (c2) bamboo, and (d2) rice straw, EDS analysis of (e) 5Mo/RBC_{1.5}, (f) 5Mo/WBC_{1.5}, (g) 5Mo/BBC₂ and (h) 5Mo/SBC₂.

regenerated by washing with acetonitrile, its desulfurization efficiency remained stable after five cycles (Fig. 7(c) blue column). ICP analysis of the spent catalyst (Table S6) showed no significant decrease in Mo content compared to the initial level, indicating excellent stability. Moreover, the biochar catalyst, with a particle size of approximately 50 μ m, can be conveniently separated from the oil phase by filtration or centrifugation, further enhancing its practicality for industrial applications.

To evaluate the versatility of the Mo-based biochar catalyst preparation method, we employed the same procedure to synthesize Mo-based catalysts from various biomass sources, including rice stalk biochar (Mo/SBC), bamboo biochar (Mo/BBC), rapeseed oil cake biochar (Mo/RBC), and walnut oil cake biochar (Mo/WBC). The desulfurization efficiencies achieved by these catalysts were 99.6%, 99.07%, 99%, and 99.1% at 10, 20, 25, and 30 min, respectively (Fig. 7(d)). The variations in catalytic times are likely due to differences in the polarities of the biochar carriers. We modulated the polarity of WBC and RBC by varying the mass of KOH used in the activation process. When the mass ratio of KOH to biochar was set to 2, the desulfurization efficiencies of 5Mo/RBC₂ and 5Mo/WBC₂ were 94.22% and 88.87%, respectively (Fig. S12). This demonstrates that the polarity of the catalyst can be fine-tuned by adjusting the KOH mass, thereby augmenting the removal rate of DBT. The

observed fluctuations in desulfurization performance likely stem from the distinct polarities of the biochar carriers, as illustrated in Fig. 8. This finding underscores the significance of carrier polarity in determining the catalytic behavior and demonstrates the potential for customizing catalyst properties to optimize performance for specific applications.

Fig. 8(a)—(d) depict SEM images of catalysts with different carriers, namely rapeseed oil cake, walnut, bamboo, and rice straw biochar, all exhibiting irregular block-like morphologies. Notably, amphiphilic catalysts, which are modified by adjusting the KOH mass during preparation, remain dispersed in the reaction medium even after 30 min of catalysis (Fig. 8(a1)—(d1)). However, following the reaction, more polar catalysts, such as 5Mo/RBC₂ and 5Mo/WBC₂, tend to settle beneath the model oil phase, which inhibits catalytic activity and lowers DBT removal efficiency (Figs. S13 and S14).

The polarity of biochar can be represented as (N + O)/C (Huang et al., 2023), is higher for WBC and RBC due to their nitrogen content, making them more polar compared to SBC and BBC. This increase in polarity can be effectively modulated by adjusting the KOH mass used in catalyst preparation (Fig. 8(e)–(h)). Experimental evidence demonstrates that this approach is broadly applicable for tuning the polarity of biochar-based catalysts in

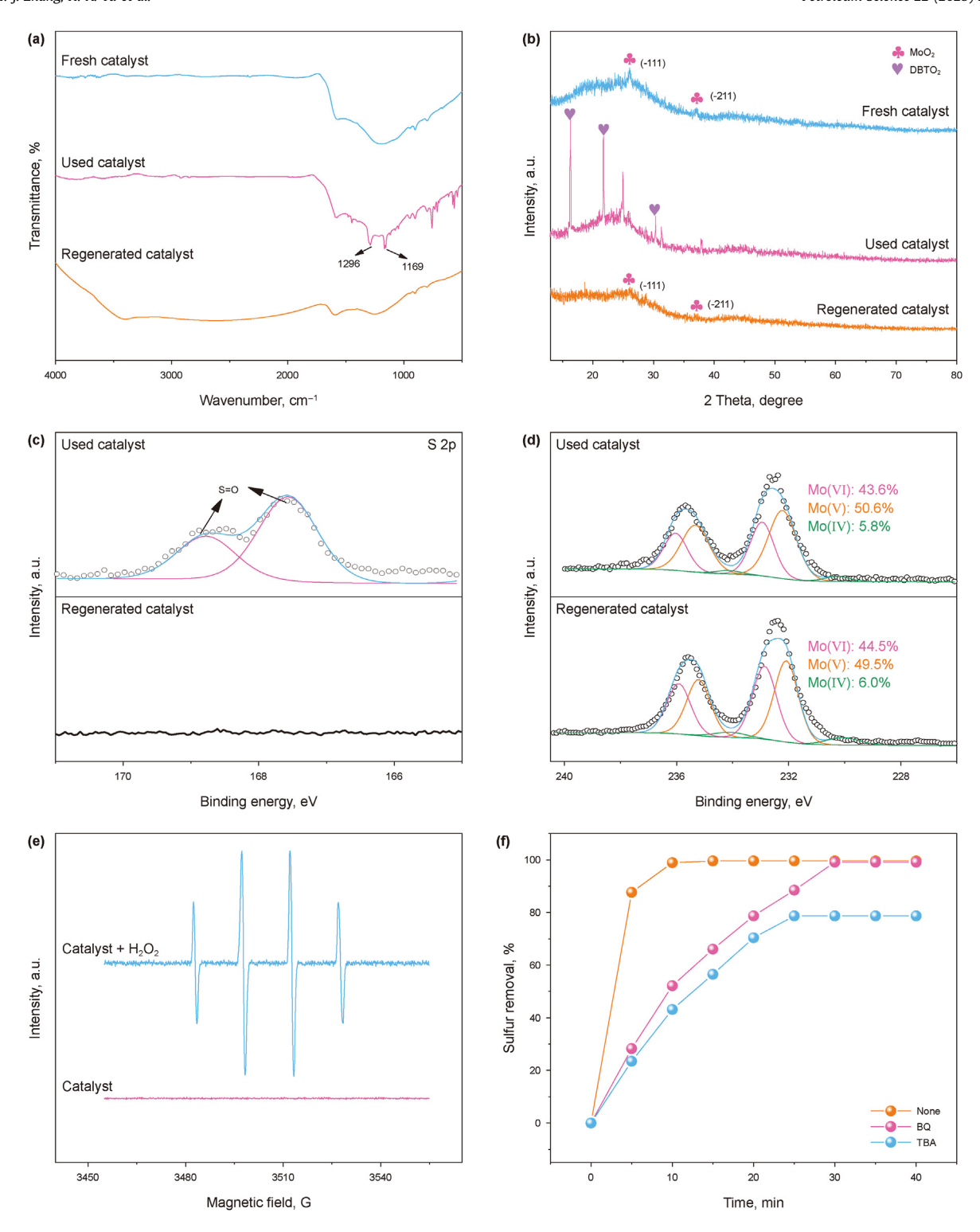


Fig. 9. (a) FT-IR spectra of fresh $5Mo/CBC_2$, used $5Mo/CBC_2$ and regenerated $5Mo/CBC_2$, (b) XRD patterns of fresh $5Mo/CBC_2$, used $5Mo/CBC_2$ and regenerated $5Mo/CBC_2$, high-resolution XPS spectra of used $5Mo/CBC_2$ and regenerated $5Mo/CBC_2$, (c) S 2p and (d) Mo 3d, (e) EPR spectra of reaction systems without H_2O_2 and with H_2O_2 , (f) radical quenching over in the ODS reaction of DBT.

extractant-free oxidative desulfurization (ODS) systems. By optimizing the polarity of the catalysts, significant improvements in desulfurization performance can be achieved, highlighting the potential of this strategy for further industrial applications.

To further validate the stability of biochar catalysts and their dual functions in catalysis and adsorption, fresh, used and

regenerated catalysts were studied by SEM, FTIR, XRD, and XPS analysis (Fig. 9 and Figs. S15–S18). No change in particle size was observed for the recovered catalyst in Fig. S15, indicating that the catalyst is stable in morphology. Compared with the FT-IR spectra of the fresh 5Mo/CBC₂ catalyst, the recovered 5Mo/CBC₂ catalyst showed two new peaks at 1169 and 1296 cm⁻¹, respectively,

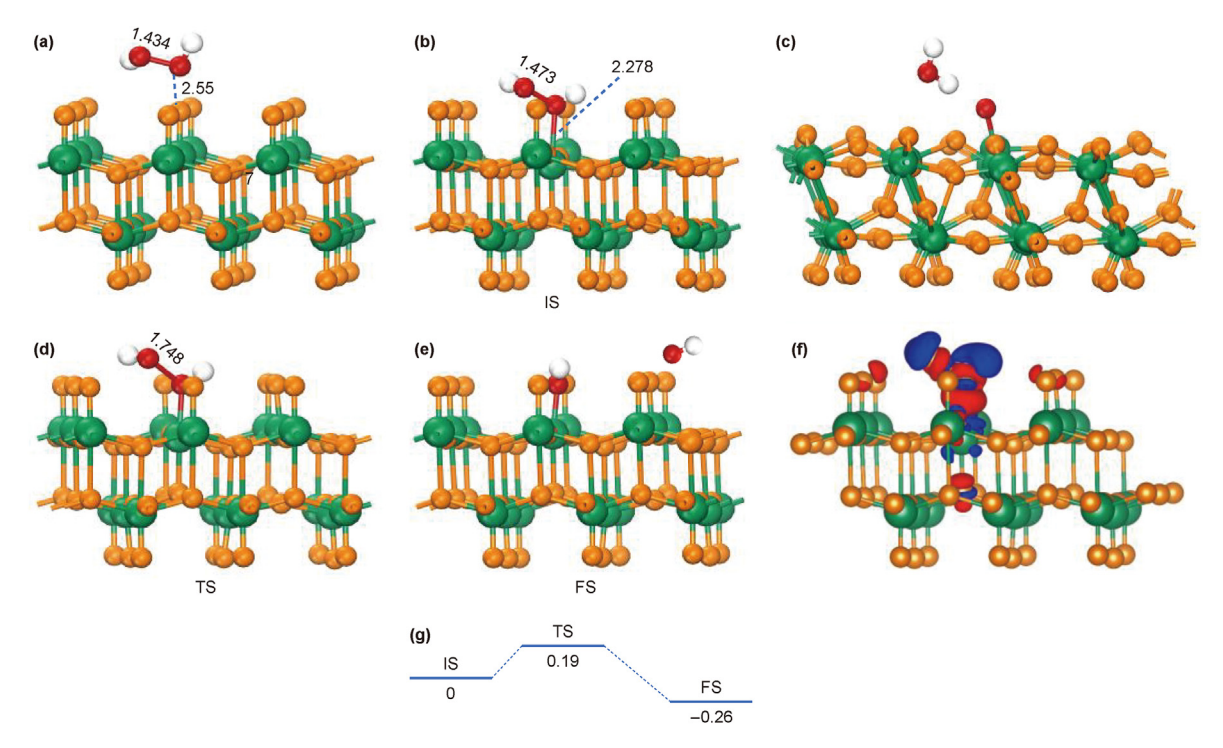
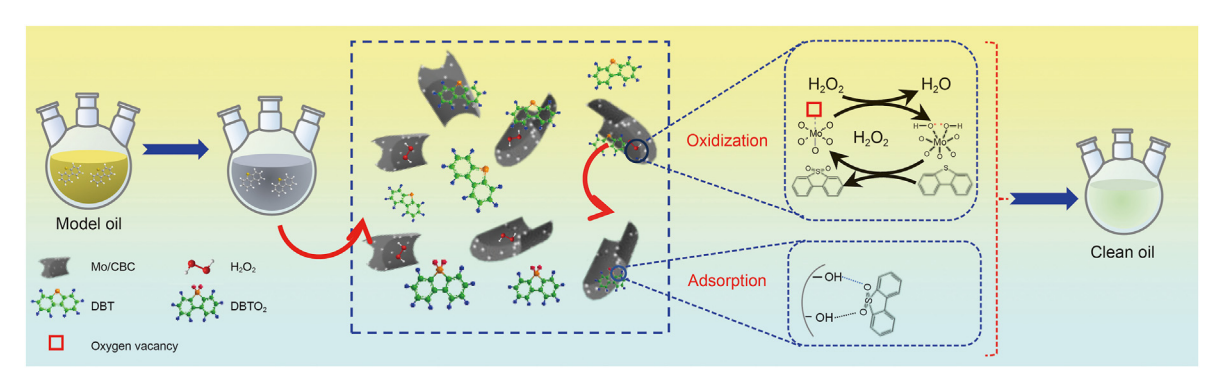


Fig. 10. The models of **(a)** H_2O_2 adsorbed on MoO_3 ; **(b)** initial state of H_2O_2 dissociation on O_{vac} - MoO_3 , and **(c)** MoO_2 ; **(d)** Transition state of H_2O_2 dissociation on O_{vac} - MoO_3 ; **(f)** Electron density difference of H_2O_2 adsorbed on O_{vac} - MoO_3 , bule and red refer to the decrease and increase of the electron densities. (Orange: O atom, green: Mo atom, white: H atom, red: O atom in H_2O_2); **(g)** The energy barrier of H_2O_2 dissociation on O_{vac} - MoO_3 .



Scheme 1. Schematic of catalytic ODS mechanism of DBT by the prepared catalysts in the presence of H₂O₂.

attributed to the symmetric and asymmetric stretching vibrations of S=O, confirming the adsorption of DBTO₂ on 5Mo/CBC₂ catalyst (Fig. 9(a)) (F. Li et al., 2022). Meanwhile, the XRD pattern also confirmed the adsorption of DBTO2 on 5Mo/CBC2 catalyst (Green pentagram represents catalyst DBTO₂ in Fig. 9(b)). These results could identify the existence of DBTO₂ in used 5Mo/CBC₂ catalyst, indicating that the biochar catalyst not only have catalytic ability, but also can adsorb the oxidized sulfur-containing compounds. Interestingly, FTIR and XRD results demonstrated that the surface functional groups of the recovered catalyst remained unchanged even after acetonitrile washing (Fig. 9(a) and (b)). In addition, the XPS spectra of 5Mo/CBC2 used showed new peaks at 167.1 and 168.8 eV, which matched well with S=O(Yao et al., 2022)(Fig. 9(c)), further confirming the formation and adsorption of DBTO₂ on the catalyst surface. After acetonitrile washing, no sulfur-containing species were detected on 5Mo/CBC2, indicating successful removal of DBTO₂. High-resolution XPS spectra of C 1s (Fig. S17), Mo 3d (Fig. 9(d)), and O 1s (Fig. S18) of the used 5Mo/CBC2

exhibited good reproducibility of the catalysts, suggesting that the oxidation reaction process rarely changed the surface properties of the catalysts. Mo (V) sites, essential for catalytic activity, remained intact even after repeated cycles. Additionally, the active Mo content remained almost unchanged post-acetonitrile washing (Table S6), explaining the consistent desulfurization efficiency after five catalytic cycles. Additionally, gas chromatography-mass spectrometry (GC-MS) was employed to monitor the catalytic oxidation process of dibenzothiophene (DBT). The mass spectrum of the simulated oil (DBT dissolved in n-octane) showed a peak at 184, corresponding to DBT (Fig. S19), while the peak at 216 of GC-MS in the oil phase after 10 min in ODS system indicated that only DBTO₂ was observed (Fig. S20). This confirms that DBT was fully oxidized to DBTO₂ in the current ODS system (F. Li et al., 2022).

3.3. ODS mechanism on Mo/CBC

To elucidate the mechanisms influencing the catalytic oxidative

desulfurization (ODS) of Mo/CBC with abundant oxygen vacancies, density functional theory (DFT) calculations were conducted. These calculations focused on the adsorption of H_2O_2 at the OVs on the MoO_{3-x} surface and the subsequent generation of \bullet OH radicals, which are critical for the ODS process. Three structural models, representing H_2O_2 adsorption on pristine MoO_3 , O_{vac} - MoO_3 , and MoO_2 were constructed and analyzed (Fig. 10(a)—(c), respectively). The adsorption energy of H_2O_2 on MoO_3 was calculated to be -0.28 eV, with an O–O bond length of 1.434 Å. However, the weak hydrogen bond formed between the H atom in H_2O_2 and the O atom in MoO_3 indicates unfavorable H_2O_2 dissociation, limiting its ability to produce reactive \bullet OH radicals.

In contrast, on MoO₂, H₂O₂ dissociates directly into H₂O and O atom on the surface, rather than generate •OH. On O_{vac}-MoO₃, oxygen defects promote the adsorption of H₂O₂, with an adsorption energy of -0.25 eV. The distance of the O-O bond is 1.473 Å, while that of O-Mo is 2.278 Å (Fig. 10(b)), indicating O atoms in H₂O₂ preferentially adsorb at the vacancy sites. Moreover, H2O2 dissociation is calculated from Fig. 10(d)-10(f). As shown in Fig. 10(d), in transition state, O-O bond is elongated to 1.748 Å, indicating the activation of O-O bond in H₂O₂. Finally, H₂O₂ dissociates into two •OH in Fig. 10(e). The charge density difference (Fig. 10(f)) reveals electron accumulation between the Mo atom and the O atom of •OH, demonstrating strong charge transfer between Mo and •OH. H₂O₂ adsorption on O_{vac}-MoO₃ occurs with a low energy barrier of 0.19 eV, suggesting favorable thermodynamics for these reactions (Fig. 10(g)). Therefore, Ovac-MoO3 is identified as the primary contributor to •OH generation, highlighting its pivotal role in the catalytic oxidative desulfurization process.

To further elucidate the mechanism for catalytic oxidative and adsorptive desulfurization, the generation of free radical species was analyzed using EPR spectroscopy using DMPO as a free radical scavenger. The EPR spectrum shows hydroxyl radicals (\bullet OH) with four line signals (Fig. 9(e)) (Zhou et al., 2023). In radical trapping experiments (Fig. 9(f)), tert-butanol (TBA) and p-benzoquinone (BQ) were used as scavengers for \bullet OH and \bullet O $_2$, respectively. When BO was added, the desulfurization rate decreased slightly, but the

final sulfur removal rate remained unaffected. This indicates that $\bullet O_2^-$ is not the primary radical species involved in the reaction. Conversely, when TBA was introduced, the desulfurization efficiency dropped significantly to 78% within 25 min, highlighting the critical role of \bullet OH radicals in the ODS reaction.

Based on the structure of MoO_{3-x} shown in Fig. 3, the oxidation process was examined. When Mo atoms exist in the form of Mo (V), oxygen vacancies chemically adsorb H_2O_2 by coordinating with Mo atoms through peroxy O-O bonds, promoting O-O bond cleavage and producing a large number of electrophilic active species $\bullet OH$ (Wang et al., 2021) (Scheme 1). These findings align with the DFT calculations, confirming that oxygen vacancies are the primary contributors to the production of active species. As a result, DBT is oxidized to DBTO₂. Additionally, the Mo (V) state promotes H_2O_2 decomposition, accelerating the reaction rate. Importantly, the catalyst exhibits excellent reusability, as it can be easily regenerated by washing with acetonitrile, demonstrating its potential for practical applications.

To evaluate the oxidative desulfurization (ODS) performance of our catalyst, we compared it with other reported amphiphilic catalysts, as summarized in Table 3. Amphiphilic catalyst carriers can be broadly classified into three categories: SiO₂, synthetic carbon, and ionic liquids. Despite the commendable catalytic performance of many previously reported catalysts, their intricate preparation methods or high operating temperatures can escalate desulfurization costs. We conducted cost analyses based on the preparation conditions and sources of the catalysts. The Mo/CBC catalyst, with its straightforward preparation and the ready availability of raw materials, distinguishes itself. Historical applications of biochar have been limited to adsorptive desulfurization due to its inherently low polarity, which impedes interaction with oxidants and stifles the reaction. Consequently, biochar has not been utilized in extractant-free catalytic oxidative desulfurization. In this study, we developed a straightforward method to modify the polarity of the biochar carrier, imparting it with amphiphilic properties. By comparing reaction time, temperature, conversion rate, and cost, we established that this catalyst is capable of catalytic oxidative

Table 3Comparison of amphiphilic catalysts for the oxidation of DBT in model fuels.

Catalyst	Carrier	Oxidant	O/S	$m_{\rm DBT}/m_{\rm catal}^{\rm a}$, mg/g	Time, min	Temp., °C	Conversion, %	Cost	Ref
HPW-NH ₂ -HHSS	SiO ₂	H ₂ O ₂	2.5	49.68	30	60	99.36	medium	Chen et al. (2020)
2D-CSx-NH ₂ -HPW		H_2O_2	3	49.85	15	60	99.7	medium	F. Li et al., (2022)
C ₁₆ N-Nb ₆ /SiO ₂		H_2O_2	5	53.33	40	60	100	high	Liu et al. (2023)
CuO/SiO ₂ @V-PIL	CuO/SiO ₂	Air	-	24.98	40	120	99.9	medium	A. Li et al., (2022)
SiO ₂ @C-dots/QPW5501	SiO ₂ @C	H_2O_2	2	73.56	120	50	98.08	medium	Zhang and Wang (2018)
GO/COOH	Synthetic Carbon	H_2O_2	-	95	300	40	95	high	Abdi et al. (2017)
TiO ₂ /MWCNTs -NH ₂ -HPW		H_2O_2	3	59.4	30	60	99	medium	Yang et al. (2021)
V _O -MoO ₃ @NPC		H_2O_2	3	49.55	20	60	99.1	medium	An et al. (2024)
Red Mud	Ionic liquids	H_2O_2	8	25	60	325	100	high	Cristina de Resende et al. (2014)
NSTS-x	-	TBHP	3	50	5	25	100	medium	Wang et al. (2019)
HPW-IL/SBA-15		H_2O_2	4	92.5	40	60	100	medium	Xiong et al. (2014)
V-PIL		CHP	5	82.5	240	40	99	medium	Chen et al. (2016)
PDD-PMo		H_2O_2	10	83.33	30	25	100	medium	Mao et al. (2023)
p-C ₂ VIM-DVB-2-PMo		H_2O_2	5	95	120	40	95	medium	Chen et al. (2023)
HPW-NH ₂ -CPRNSs	CPRNSs	H_2O_2	6	42.38	90	60	98.9	medium	Zhang et al. (2022)
GB-W ₁₈ O ₄₉	W ₁₈ O ₄₉	O_2	130	48.85	300	130	97.7	high	Xiong et al. (2022)
Mo/HEPO-SAC	HEPO-SAC	Air	-	200	60	120	almost 100%	medium	Liu J. et al. (2023a)
MoO ₃ /La ₂ O ₂ CO ₃	$La_2O_2CO_3$	O_2	-	200	150	130	100	high	Shao et al. (2024)
Mo/HNT/S	HNT	H_2O_2	4	62.5	15	60	100	medium	Guo et al. (2023a)
5Mo/CBC ₂	Biochar	H_2O_2	6	59.76	10	60	99.6	low	This work
5Mo/BBC ₂		H_2O_2	6	59.46	20	60	99.1	low	
5Mo/SBC ₂		H_2O_2	6	59.76	15	60	99.6	low	
5Mo/WBC _{1.5}		H_2O_2	6	59.46	30	60	99.1	low	
5Mo/RBC _{1.5}		H_2O_2	6	59.76	20	60	99	low	

^a $m_{\text{DBT}}/m_{\text{catal}} = \frac{C_0 \cdot V \cdot \eta}{m}$, C_0 represents the initial concentration of DBT, m_g/L , V represents the model oil volume, L, η Represents the conversion rate of DBT, %, and m represents the amount of catalyst used, g.

desulfurization under extractant-free and mild reaction conditions. This positions our catalyst as one of the most effective and economically viable options currently available.

4. Conclusion

In summary, we have successfully synthesized a suite of dualfunction amphiphilic Mo-based biochar catalysts optimized for extractant-free catalytic oxidative desulfurization (ODS). These catalysts showcase outstanding dispersibility in both oil and water phases, eliminating the need for a separate extraction phase in the desulfurization process. Their ODS performance was comprehensively evaluated across a range of systems, demonstrating superior efficiency under mild reaction conditions. The amorphous regions generated during ball milling augmented surface energy, which in turn promoted the loading of the active site MoO_{3-x}. Furthermore, the diminutive particle size of the catalysts curtailed the mass transfer path of the reactants, thereby augmenting the mass transfer rate. Precise control over the calcination temperature enabled the biochar carrier to form abundant oxygen vacancies through carbon reduction, which contributed to the catalysts' high catalytic activity and durability across multiple ODS cycles. The catalysts exhibited robust cycling stability, with minimal loss of performance after five cycles. The ODS system followed pseudofirst-order kinetics, and the role of •OH radicals was confirmed through radical trapping experiments and EPR spectroscopy. Various biomass sources, including rice stalk biochar, bamboo biochar, rapeseed oil cake biochar, were utilized to prepare dualfunction amphiphilic Mo-based biochar catalysts. All demonstrated outstanding desulfurization performance, underscoring the versatility of this approach. Leveraging agricultural waste biochar to develop dual-function catalysts capable of both oxidation and adsorption offers a versatile, environmentally friendly, and costeffective solution for one-step fuel desulfurization. This strategy not only provides a sustainable pathway for utilizing agricultural waste but also establishes a new benchmark for efficient and practical desulfurization processes.

CRediT authorship contribution statement

Xue Liang: Writing — original draft, Validation, Methodology, Investigation, Formal analysis, Data curation, Conceptualization. Tian-Jing Zhang: Validation, Investigation, Formal analysis. Hong-Xia Yu: Validation, Methodology, Formal analysis. Jie Hong: Writing — review & editing, Validation. Mohamed Abbas: Writing — review & editing, Validation. Claudia Li: Writing — review & editing, Validation, Sibudjing Kawi: Writing — review & editing, Validation, Methodology. Wan-Liang Yang: Writing — review & editing, Validation, Supervision, Resources, Project administration, Methodology, Funding acquisition, Conceptualization. Mei-Song Xu: Writing — review & editing, Supervision, Resources, Methodology.

Declaration of interest statement

The authors declare that they have no known competing financial interests or personal relationships that could have appeared to influence the work reported in this paper.

Acknowledgements

This work was supported by the National Natural Science Foundation of China (22162008), the Science and Technology Supporting Project of Guizhou Province ([2022]208), the Guizhou Province Local Government Overseas Study Program, and the open

project of Guizhou Provincial Double Carbon and Renewable Energy Technology Innovation Research Institute.

Appendix A. Supplementary data

Supplementary data to this article can be found online at https://doi.org/10.1016/j.petsci.2025.02.021.

References

- Abdi, G., Ashokkumar, M., Alizadeh, A., 2017. Ultrasound-assisted oxidative-adsorptive desulfurization using highly acidic graphene oxide as a catalyst-adsorbent. Fuel 210, 639–645. https://doi.org/10.1016/j.fuel.2017.09.024.
- Afshar, M., Mofatteh, S., 2024. Biochar for a sustainable future: environmentally friendly production and diverse applications. Rineng 23, 102433. https://doi.org/10.1016/j.rineng.2024.102433.
- Ahmad, M., Lee, S.S., Dou, X., et al., 2012. Effects of pyrolysis temperature on soybean stover- and peanut shell-derived biochar properties and TCE adsorption in water. Bioresour. Technol. 118, 536–544. https://doi.org/10.1016/j.biortech.2012.05.042.
- An, X., Gao, X., Yin, J., et al., 2024. MOF-derived amorphous molybdenum trioxide anchored on nitrogen-doped porous carbon by facile in situ annealing for efficient oxidative desulfurization. Chem. Eng. J. 480, 147879. https://doi.org/ 10.1016/j.cej.2023.147879.
- Brocza, F.M., Foster, S.J., Peacock, C.L., et al., 2024. Synthesis and applications of manganese oxide - biochar composites: a systematic review across catalysis, capacitor and sorption applications. Biomass Bioenergy 184, 107201. https:// doi.org/10.1016/i.biombioe.2024.107201.
- Castro, I.A.d., Datta, R.S., Ou, J.Z., et al., 2017. Molybdenum oxides from fundamentals to functionality. Adv. Mater. 29 (40), 1701619. https://doi.org/10.1002/adma.2017.01619
- Chang, X., Yang, X., Qiao, Y., et al., 2020. Confined heteropoly blues in defected Zr-MOF (bottle around ship) for high-efficiency oxidative desulfurization. Small 16 (14), 201906432. https://doi.org/10.1002/smll.201906432.
- Chen, H., Hou, S., Cui, H., et al., 2023. Construction of amphiphilic and poly-oxometalate poly(ionic liquids) for enhanced oxidative desulfurization in fuel. J. Mol. Liq. 379, 121650. https://doi.org/10.1016/j.molliq.2023.121650.
- Chen, J., Zhou, J., Zheng, W., et al., 2024. A complete review on the oxygencontaining functional groups of biochar: formation mechanisms, detection methods, engineering, and applications. Sci. Total Environ. 946, 174081. https:// doi.org/10.1016/j.scitotenv.2024.174081.
- Chen, L., Yuan, Z.Y., 2022. Design strategies of supported metal-based catalysts for efficient oxidative desulfurization of fuel. J. Ind. Eng. Chem. 108, 1–14. https:// doi.org/10.1016/j.jiec.2021.12.025.
- Chen, M., Cui, J., Wang, Y., et al., 2020. Amine modified nano-sized hierarchical hollow system for highly effective and stable oxidative-adsorptive desulfurization. Fuel 266, 116960. https://doi.org/10.1016/j.fuel.2019.116960.
- Chen, Y., Song, H., Lu, Y., et al., 2016. Unified catalytic oxidation—adsorption desulfurization process using cumene hydroperoxide as oxidant and vanadate based polyionic liquid as catalyst and sorbent. Ind. Eng. Chem. Res. 55 (39), 10394—10403. https://doi.org/10.1021/acs.iecr.6b02464.
- Cristina de Resende, E., Carvalho, I.d.R.G., Schlaf, M., et al., 2014. Red Mud waste from the Bayer process as a catalyst for the desulfurization of hydrocarbon fuels. RSC Adv. 4 (88), 47287—47296. https://doi.org/10.1039/C4RA07635D.
- Di, J., Chen, C., Zhu, C., et al., 2021. Surface local polarization induced by bismuth-oxygen vacancy pairs tuning non-covalent interaction for CO₂ photoreduction. Adv. Energy Mater. 11 (41), 202102389. https://doi.org/10.1002/aenm.202102389.
- Dissanayake, P.D., Choi, S.W., Igalavithana, A.D., et al., 2020. Sustainable gasification biochar as a high efficiency adsorbent for CO₂ capture: a facile method to designer biochar fabrication. Renew. Sustain. Energy Rev. 124, 109785. https://doi.org/10.1016/j.rser.2020.109785.
- Dou, J., Zeng, H., 2014. Integrated networks of mesoporous silica nanowires and their bifunctional catalysis-sorption application for oxidative desulfurization. ACS Catal. 4 (2), 566–576. https://doi.org/10.1021/cs400996j.
- Feng, L., Yu, H., Yang, G., et al., 2023. Novel 3D@2D/2D HHSS@BiOBr/Znln₂S₄ S-scheme photocatalyst for efficient adsorption-photocatalytic-photosensitization synergistic degradation of organics. Appl. Surf. Sci. 640, 158340. https://doi.org/10.1016/j.apsusc.2023.158340.
- Ganiyu, S.A., Lateef, S.A., 2021. Review of adsorptive desulfurization process: overview of the non-carbonaceous materials, mechanism and synthesis strategies. Fuel 294, 120273. https://doi.org/10.1016/j.fuel.2021.120273.
- Guo, J., Chu, L., Yang, H., et al., 2023a. Amphiphilic halloysite nanotube enclosing molybdenum oxide as nanoreactor for efficient desulfurization of model fuels. Chem. Eng. J. 451, 138595. https://doi.org/10.1016/j.cej.2022.138595.
- Guo, J., Li, B., Zhao, D., et al., 2023b. Preparation of porous hollow spherical MoO_X/C catalyst for efficient extraction and oxidative desulfurization. Chem. Eng. J. 474, 145853. https://doi.org/10.1016/j.cej.2023.145853.
- Hao, L., Sun, L., Su, T., et al., 2019. Polyoxometalate-based ionic liquid catalyst with unprecedented activity and selectivity for oxidative desulfurization of diesel in [Omim]BF₄. Chem. Eng. J. 358, 419–426. https://doi.org/10.1016/ j.cej.2018.10.006.

Huang, Y., Huang, Y., Fang, L., et al., 2023. Interfacial chemistry of mercury on thiol-modified biochar and its implication for adsorbent engineering. Chem. Eng. J. 454, 140310. https://doi.org/10.1016/j.cej.2022.140310.

- Jiang, W., Xiao, J., Dong, L., et al., 2019. Polyoxometalate-based poly(ionic liquid) as a precursor for superhydrophobic magnetic carbon compositecatalysts toward aerobic oxidative desulfurization. ACS Sustain. Chem. Eng. 7 (18), 15755–15761. https://doi.org/10.1021/acssuschemeng.9b04026.
- Jiang, W., Xiao, J., Gao, X., et al., 2021. In situ fabrication of hollow silica confined defective molybdenum oxide for enhanced catalytic oxidative desulfurization of diesel fuels, Fuel 305, 121470. https://doi.org/10.1016/j.fuel.2021.121470.
- Julião, D., Mirante, F., Ribeiro, S.O., et al., 2019. Deep oxidative desulfurization of diesel fuels using homogeneous and SBA-15-supported peroxophosphotungstate catalysts. Fuel 241, 616–624. https://doi.org/10.1016/j.fuel.2018.11.095.
- Koohsaryan, E., Anbia, M., Heydar, K.T., 2022. Mo-modified hierarchical FAU zeolite: a catalyst-adsorbent for oxidative desulfurization of fuel oil. J. Solid State Chem. 312, 123218. https://doi.org/10.1016/j.jssc.2022.123218.
- Kuwahara, Y., Furuichi, N., Seki, H., et al., 2017. One-pot synthesis of molybdenum oxide nanoparticles encapsulated in hollow silica spheres: an efficient and reusable catalyst for epoxidation of olefins. J. Mater. Chem. A 5 (35), 18518–18526. https://doi.org/10.1039/c7ta06288e.
- Li, A., Song, H., Meng, H., et al., 2022. Peroxovanadic based core-shell bifunctional poly(ionic liquid)s catalyst CuO/SiO₂@V-PIL: its in-situ free radical initiation mechanism for air oxidative desulfurization. Fuel 310, 122430. https://doi.org/10.1016/i.fuel.2021.122430.
- Li, F., Zhou, W., Yang, W., et al., 2022. Design of hierarchical self-assembly 2D silica and their derivative catalysts with accessible open transport channels for boosting oxidative-adsorptive desulfurization in fuel oil. Fuel 324, 124403. https://doi.org/10.1016/j.fuel.2022.124403.
- Liang, Y., Xiong, C., Zhou, X., et al., 2023. Preparation of Mo-based catalyst appreciated from agricultural waste for efficient high-value conversion of 1-hexene. Chem. Eng. J. 455, 140648. https://doi.org/10.1016/j.cej.2022.140648.
- Liu, F., Yu, J., Qazi, A.B., et al., 2021. Metal-based ionic liquids in oxidative desulfurization: a critical review. Environ. Sci. Technol. 55 (3), 1419–1435. https:// doi.org/10.1021/acs.est.0c05855.
- Liu, H., Liu, C., Zhen, N., et al., 2023. Amphiphilic polyoxoniobate-based recoverable Pickering emulsion for effective oxidative desulfurization. Appl. Catal. A-gen. 656, 119133. https://doi.org/10.1016/j.apcata.2023.119133.
- Liu, J., Deng, C., Liu, X., et al., 2023a. Single Mo atoms stabilized on high-entropy perovskite oxide: a frontier for aerobic oxidative desulfurization. Inorg. Chem. 62 (28), 11044–11055. https://doi.org/10.1021/acs.inorgchem.3c01085.
- Liu, J., Liu, X., Yan, R., et al., 2023b. Active phase morphology engineering of NiMo/Al₂O₃ through La introduction for boosting hydrodesulfurization of 4,6-DMDBT. Pet. Sci. 20 (2), 1231–1237. https://doi.org/10.1016/j.petsci.2022.09.023.
- Liu, Y., Han, L., Zhang, J., et al., 2020. Morphology-controlled construction and aerobic oxidative desulfurization of hierarchical hollow Co-Ni-Mo-O mixed metal-oxide nanotubes. Ind. Eng. Chem. Res. 59 (14), 6488–6496. https:// doi.org/10.1021/acs.iecr.9b06988.
- Liu, Y., Wang, F., Lv, Y., et al., 2021. Three-dimensional graphene oxide covalently functionalized with dawson-type polyoxotungstates for oxidative desulfurization of model fuels. Ind. Eng. Chem. Res. 60 (1), 114–127. https://doi.org/ 10.1021/acs.iecr.0c04384.
- Liu, Z., Zhang, Y., Bai, J., et al., 2023c. MoO_X nanoclusters decorated on spinel-type transition metal oxide porous nanosheets for aerobic oxidative desulfurization of fuels. Fuel 334, 126753. https://doi.org/10.1016/j.fuel.2022.126753.
- Lu, J., Yang, Y., Liu, P., et al., 2020. Iron-montmorillonite treated corn straw biochar: interfacial chemical behavior and stability. Sci. Total Environ. 708, 134773. https://doi.org/10.1016/j.scitotenv.2019.134773.
- Luo, G., Kang, L., Zhu, M., et al., 2014. Highly active phosphotungstic acid immobilized on amino functionalized MCM-41 for the oxidesulfurization of dibenzothiophene. Fuel Process. Technol. 118, 20–27. https://doi.org/10.1016/j.fuproc.2013.08.001.
- Mao, S., Song, J., Zhu, W., et al., 2023. Heterogeneous oxidative desulfurization of fuels using amphiphilic mesoporous phosphomolybdate-based poly(ionic liquid) over a wide temperature range. Fuel 352, 128982. https://doi.org/ 10.1016/j.fuel.2023.128982.
- Marafi, A., Albazzaz, H., Rana, M.S., 2019. Hydroprocessing of heavy residual oil: opportunities and challenges. Catal. Today 329, 125–134. https://doi.org/ 10.1016/j.cattod.2018.10.067.
- McNamara, N.D., Neumann, G.T., Masko, E.T., et al., 2013. Catalytic performance and stability of (V) MIL-47 and (Ti) MIL-125 in the oxidative desulfurization of heterocyclic aromatic sulfur compounds. J. Catal. 305, 217–226. https://doi.org/ 10.1016/j.jcat.2013.05.021.
- Nascimento, C.T.d., Vieira, M.G.A., Scheufele, F.B., et al., 2022. Adsorption of atrazine from aqueous systems on chemically activated biochar produced from corn straw. J. Environ. Chem. Eng. 10 (1), 107039. https://doi.org/10.1016/ i.jece.2021.107039.
- Rajapaksha, A.U., Chen, S.S., Tsang, D.C.W., et al., 2016. Engineered/designer biochar for contaminant removal/immobilization from soil and water: potential and implication of biochar modification. Chemosphere 148, 276–291. https:// doi.org/10.1016/j.chemosphere.2016.01.043.
- Rajendran, A., Cui, T., Fan, H., et al., 2020. A comprehensive review on oxidative desulfurization catalysts targeting clean energy and environment. J. Mater. Chem. A 8 (5), 2246–2285. https://doi.org/10.1039/c9ta12555h.
- Rajendran, A., Fan, H., Cui, T., et al., 2022. Octamolybdates containing Mo^V and Mo^{VI} sites supported on mesoporous tin oxide for oxidative desulfurization of liquid

fuels. J. Clean. Prod. 334, 130199. https://doi.org/10.1016/j.jclepro.2021.130199.

- Safa, M.A., Ma, X., 2016. Oxidation kinetics of dibenzothiophenes using cumene hydroperoxide as an oxidant over MoO₃/Al₂O₃ catalyst. Fuel 171, 238–246. https://doi.org/10.1016/j.fuel.2015.12.050.
- Shao, S., Liu, H., Wang, X., et al., 2024. Unveiling the structure-performance of MoO₃/La₂O₂CO₃ for ultra-deep aerobic oxidative desulfurization of diesel. Chem. Eng. J. 495, 153654. https://doi.org/10.1016/j.cej.2024.153654.
- Song, L., Yuan, Y., Wang, Y., et al., 2024. Cu-MOF-derived Cu nanoparticles decorated porous N-doped biochar for low-temperature H₂S desulfurization. Fuel 368, 131682. https://doi.org/10.1016/j.fuel.2024.131682.
- Su, J., Zhang, M., Xu, W., et al., 2024. Preparation and applications of iron/biochar composites in remediation of heavy metal contaminated soils: current status and further perspectives. Environ. Technol. Innov. 35, 103671. https://doi.org/ 10.1016/i.eti.2024.103671.
- Sun, L., Su, T., Xu, J., et al., 2019. Aerobic oxidative desulfurization coupling of Co polyanion catalysts and p-TsOH-based deep eutectic solvents through a biomimetic approach. Green Chem. 21 (10), 2629–2634. https://doi.org/10.1039/c8gc03941k.
- Torres-García, E., Galano, A., Rodriguez-Gattorno, G., 2011. Oxidative desulfurization (ODS) of organosulfur compounds catalyzed by peroxo-metallate complexes of WOx–ZrO2: thermochemical, structural, and reactivity indexes analyses. J. Catal. 28 (1), 201–208. https://doi.org/10.1016/j.jcat.2011.06.010. Ullah, F., Ji, G., Irfan, M., et al., 2022. Adsorption performance and mechanism of
- Ullah, F., Ji, G., Irfan, M., et al., 2022. Adsorption performance and mechanism of cationic and anionic dyes by KOH activated biochar derived from medical waste pyrolysis. Environ. Pollut. 314, 120271. https://doi.org/10.1016/ i.envpol.2022.120271.
- Wang, H., Shi, C., Chen, S., et al., 2019. Hierarchically mesoporous Titanosilicate single-crystalline nanospheres for room temperature oxidative—adsorptive desulfurization. ACS Appl. Nano Mater. 2 (10), 6602–6610. https://doi.org/ 10.1021/acsanm.9b01496.
- Wang, J., Yang, B., Peng, X., et al., 2022. Design and preparation of polyoxometalatebased catalyst [MIMPs]₃PMo₆W₆O₄₀ and its application in deep oxidative desulfurization with excellent recycle performance and low molar O/S ratio. Chem. Eng. J. 429, 132446. https://doi.org/10.1016/j.cej.2021.132446.
- Chem. Eng. J. 429, 132446. https://doi.org/10.1016/j.cej.2021.132446.

 Wang, S., Zhang, X., Chang, X., et al., 2021. Rational design of ionic V-MOF with confined Mo species for highly efficient oxidative desulfurization. Appl. Catal. B Environ. 298, 120594. https://doi.org/10.1016/j.apcatb.2021.120594.
- Wang, X., Liu, X., Tong, Y., et al., 2023. Oxygen vacancies-dominated reactive species generation from peroxymonosulfate activated by MoO_{3-x} for pollutant degradation. J. Hazard Mater. 458, 131798. https://doi.org/10.1016/j.jhazmat.2023.131798.
- Wang, Y., Hua, M., Zhou, S., et al., 2024. Regulating the coordination environment of surface alumina on NiMo/Al₂O₃ to enhance ultra-deep hydrodesulfurization of diesel. Appl. Catal. B Environ. 357, 124265. https://doi.org/10.1016/j.apcatb.2024.124265.
- Xiao, X., Song, H., Lin, S., et al., 2016. Scalable salt-templated synthesis of twodimensional transition metal oxides. Nat. Commun. 7, 11296. https://doi.org/ 10.1038/ncomms11296.
- Xie, S., Zhao, X., Bai, J., et al., 2023. Co,N-codoped MoO_x nanoclusters on graphene derived from polyoxometalate for highly efficient aerobic oxidation desulfurization of diesel. J. Catal. 428, 115186. https://doi.org/10.1016/j.jcat.2023.115186.
- Xiong, J., Li, J., Chen, C., et al., 2022. Universal strategy engineering grain boundaries for catalytic oxidative desulfurization. Appl. Catal. B Environ. 317, 121714. https://doi.org/10.1016/j.apcatb.2022.121714.
- Xiong, J., Zhu, W., Ding, W., et al., 2014. Phosphotungstic acid immobilized on ionic liquid-modified SBA-15: efficient hydrophobic heterogeneous catalyst for oxidative desulfurization in fuel. Ind. Eng. Chem. Res. 53 (51), 19895—19904. https://doi.org/10.1021/ie503322a.
- Yang, C., Jin, Q., Zhang, H., et al., 2009. Tetra-(tetraalkylammonium)octamolybdate catalysts for selective oxidation of sulfides to sulfoxides with hydrogen peroxide. Green Chem. 11 (9), 1401–1405. https://doi.org/10.1039/b912521n.
- Yang, E., Yao, C., Liu, Y., et al., 2018. Bamboo-derived porous biochar for efficient adsorption removal of dibenzothiophene from model fuel. Fuel 211, 121–129. https://doi.org/10.1016/j.fuel.2017.07.099.
- Yang, G., Zhang, X., Yang, H., et al., 2018. Sucrose facilitated synthesis of mesoporous silicoaluminophosphate SAPO-11 with different crystalline phases of MoO₃ for highly-efficient oxidative desulfurization. J. Colloid Interface Sci. 532, 92–102. https://doi.org/10.1016/j.jcis.2018.07.074.
- Yang, P., Huang, Y., Zhang, Z., et al., 2020. Shape-controlled synthesis of the metalorganic framework MIL-125 towards a highly enhanced catalytic performance for the oxidative desulfurization of 4,6-dimethyldibenzothiophene. Dalton Trans. 49 (29), 10052–10057. https://doi.org/10.1039/d0dt01955k.
- Yang, X., Yang, W., Zhang, Y., et al., 2021. Constructing dual-function TiO₂/MWCNTs-NH₂-HPW composites as both catalysts and adsorbents for highly efficient oxidative adsorption desulfurization in fuel oil. Energy Fuel. 35 (24), 20000–20015. https://doi.org/10.1021/acs.energyfuels.1c02831.
- Yao, Y., Hu, H., Zheng, H., et al., 2022. Nonprecious bimetallic Fe, Mo-embedded N-enriched porous biochar for efficient oxidation of aqueous organic contaminants. J. Hazard Mater. 422, 126776. https://doi.org/10.1016/j.jhazmat.2021.126776.
- Ye, G., Wang, H., Chen, W., et al., 2021. In situ implanting of single tungsten sites into defective UiO-66(Zr) by solvent-free route for efficient oxidative desulfurization at room temperature. Angew. Chem. Int. Ed. 60 (37), 20318–20324. https:// doi.org/10.1002/anie.202107018.
- Ye, J., Wen, J., Zhao, D., et al., 2020. Macroporous 3D carbon-nitrogen (CN) confined

- MoOx catalyst for enhanced oxidative desulfurization of dibenzothiophene. Chin. Chem. Lett. 31 (10), 2819–2824. https://doi.org/10.1016/i.cclet.2020.08.004
- Yuan, Y., Huang, L., Yılmaz, M., et al., 2023. MgFe₂O₄-loaded N-doped biochar derived from waste cooked rice for efficient low-temperature desulfurization of H₂S. Fuel 339, 127385. https://doi.org/10.1016/j.fuel.2022.127385.
- Zhang, H., Zhang, Q., Qian, G., et al., 2024. In situ synthesis of mesoporous NiS₂-MoS₂ sphere-flower hybrid for hydrodesulfurization of thiophene and 4,6-dimethyl-dibenzothiophene. J. Catal. 429, 115255. https://doi.org/10.1016/j.jcat.2023.115255.
- Zhang, S., Wang, G., Jin, J., et al., 2017. Self-catalyzed decomposition of discharge products on the oxygen vacancy sites of MoO₃ nanosheets for low-overpotential Li-O₂ batteries. Nano Energy 36, 186–196. https://doi.org/10.1016/i.nanoen.2017.04.038.
- Zhang, T., Liang, X., Zhao, H., et al., 2023. LaVO₄: Eu³⁺ nano-islands onto silica for achieving fluorescence enhancement and their detection of Fe³⁺ ions and anti-counterfeiting applications. J. Colloid Interface Sci. 652 (Pt A), 952–962. https://doi.org/10.1016/j.jcis.2023.08.065.
- Zhang, Y., Wang, R., 2018. Synthesis of silica@C-dots/phosphotungstates core-shell microsphere for effective oxidative-adsorptive desulfurization of

- dibenzothiophene with less oxidant. Appl. Catal. B Environ. 234, 247–259. https://doi.org/10.1016/j.apcatb.2018.04.031.
- Zhang, Y., Yang, W., Yang, X., et al., 2022. Rational design of efficient polar heterogeneous catalysts for catalytic oxidative-adsorptive desulfurization in fuel oil. Appl. Catal. A-gen. 632, 118498. https://doi.org/10.1016/j.apcata.2022.118498.
- Zhao, L., Zhang, Y., Wang, L., et al., 2022. Effective removal of Hg(II) and MeHg from aqueous environment by ball milling aided thiol-modification of biochars: effect of different pyrolysis temperatures. Chemosphere 294, 133820. https://doi.org/10.1016/j.chemosphere.2022.133820.
- Zhou, C., Li, F., Wang, C., et al., 2023. Constructing 2D channel catalysts with accessible open transport channels for boosting epoxidation of methyl oleate. Mol. Catal. 547, 113406. https://doi.org/10.1016/j.mcat.2023.113406.
- Zhou, S., Liu, Y., Zhu, J., et al., 2024a. Modulating hydrogen spillover effect to boost ultradeep hydrodesulfurization of 4,6-dimethyldibenzothiophene over Pt-Ni₂P/Al₂O₃. Sep. Purif. Technol. 351, 128095. https://doi.org/10.1016/j.seppur.2024.128095.
- Zhou, S., Wu, Z., Liu, J., et al., 2024b. Modifying the active phase structure of Ni₂P/Al₂O₃ by Ga introduction for improved hydrodesulfurization of diesel. Chem. Eng. J. 479, 147776. https://doi.org/10.1016/j.cej.2023.147776.